BRNO UNIVERSITY OF TECHNOLOGY

Faculty of Electrical Engineering
and Communication

# MASTER'S THESIS

Brno, 2023 Bc. Zuzana Koščová

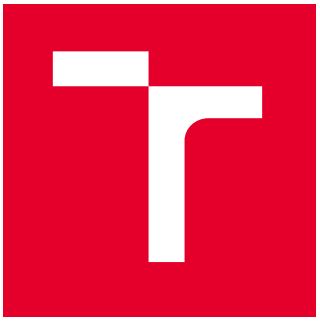


# BRNO UNIVERSITY OF TECHNOLOGY

VYSOKÉ UČENÍ TECHNICKÉ V BRNĚ

## FACULTY OF ELECTRICAL ENGINEERING AND COMMUNICATION

FAKULTA ELEKTROTECHNIKY
A KOMUNIKAČNÍCH TECHNOLOGIÍ

## DEPARTMENT OF BIOMEDICAL ENGINEERING

ÚSTAV BIOMEDICÍNSKÉHO INŽENÝRSTVÍ


# ANALYSIS OF ULTRA-HIGH FREQUENCY ECG USING DEEP LEARNING

ANALÝZA VYSOKOFREKVENČNÍHO EKG S VYUŽITÍM HLUBOKÉHO UČENÍ

**MASTER'S THESIS**
DIPLOMOVÁ PRÁCE


**AUTHOR** — **Bc. Zuzana Koščová**
AUTOR PRÁCE

**SUPERVISOR** — **Ing. Filip Plešinger, Ph.D.**
VEDOUCÍ PRÁCE



**BRNO 2023**

BRNO UNIVERSITY OF TECHNOLOGY
FACULTY OF ELECTRICAL ENGINEERING AND COMMUNICATION

# Master's Thesis

Master's study program **Biomedical Engineering and Bioinformatics**

Department of Biomedical Engineering

***Student:*** Bc. Zuzana Koščová ***ID:*** 203197

***Year of study:*** 2 ***Academic year:*** 2022/23

**TITLE OF THESIS:**

## Analysis of ultra-high frequency ECG using deep learning

**INSTRUCTION:**

1) Familiarize yourself with the issue of ventricular activation disorders (especially LBBB, RBBB, and their variants) and current therapeutic options. 2) Familiarize yourself with the analysis of the ultra-high-frequency ECG signal (UHF-ECG) concerning these disorders and related therapy. 3) From tasks 1 and 2, build the research part of the thesis. 4) Design, implement, and test a deep learning model suitable for the detection of QRS complexes in UHF-ECG. Consider the possibility of simultaneous detection of QRS duration. 5) Develop a deep learning model for removing pacemaker stimuli in the UHF-ECG signals. Furthermore, develop a deep learning regression model for direct detection of the value of ventricular electrical dyssynchrony from the UHF-ECG signals. 6) Evaluate and discuss the contribution of these models to the current state of the art of UHF-ECG analysis. To develop these models, use UHF-ECG recordings from the databases of the Institute of Scientific Instruments of the CAS and its partners.

**RECOMMENDED LITERATURE:**

[1] Jurak et al., Ventricular dyssynchrony assessment using ultra-high frequency ECG technique, Journal of Interventional Cardiac Electrophysiology, Volume 49, Issue 3, 2017, DOI:10.1007/s10840-017-0268-0
[2] Plesinger et al., Ventricular Electrical Delay Measured From Body Surface ECGs Is Associated With Cardiac Resynchronization Therapy Response in Left Bundle Branch Block Patients From the MADIT-CRT Trial, Circulation: Arrhythmia and Electrophysiology, 2018, DOI:10.1161/CIRCEP.117.005719

***Date of project specification:*** 6.2.2023 ***Deadline for submission:*** 22.5.2023

***Supervisor:*** Ing. Filip Plešinger, Ph.D.

**prof. Ing. Valentine Provazník, Ph.D.**
Chair of study program board

# ABSTRACT

Ultra-high-frequency ECG (UHF-ECG) analysis provides information about electrical ventricular dyssynchrony. Additionally, real-time UHF-ECG analysis enables direct optimization of the pacing electrode during pacemaker implantation. In this master thesis, we describe ventricular conduction abnormalities, the current method for UHF-ECG analysis and most importantly, we have developed several deep learning models to find out which steps of UHF-ECG analysis can be replaced by deep learning. Data used for the development and validation of the models come from 2 private hospitals (FNUSA-ICRC hospital, Brno, Czechia, and FNKV hospital Prague, Czechia) and from 3 publicly available datasets.

First, we present two deep learning methods for QRS complex detection and QRS complex duration estimation in one inference step. We received an overall F1-score of 98.84 $\pm$ 0.51 % for the detection task and a Mean Absolute Error (MAE) of 12.25 $\pm$ 2.16 ms for the QRS duration estimation task. This method enhances UHF-ECG analysis performance and therefore could significantly reduce measurement time.

Furthermore, a regression model for pacing stimuli removal based on a conditional generative adversarial network was developed. The results were evaluated based on the correlation of 15 averaged high-frequency envelopes in the QRS complex region between the model output and the target signal. The results show a higher correlation on spontaneous than on paced data and a drop in correlation with the increasing frequency band.

Last, two deep learning models with convolutional neural network (CNN) were created to estimate ventricular electrical dyssynchrony (VED). Specifically, 1 Dimensional (1D) and 2 Dimensional (2D) CNN. The MAE between our solution and annotation is 12.61 $\pm$18.95 ms and 12.27 $\pm$17.73 ms for 1D and 2D CNN, respectively. MAE on spontaneous data is approximately 5 ms lower than on paced data for both models, indicating the need to remove the pacing stimuli.

These deep learning models yield a reduction in the pre-processing pipeline while delivering output in a single inference step. For the QRS detection and QRS duration estimation model, the performance improvement over the current solution is evident and these steps of UHF-ECG analysis could be replaced by deep learning. However, for the removal of pacing stimuli and VED parameter estimation, it is required to improve the performance for a real use.



# KEYWORDS

ECG, UHF-ECG, deep learning, UNet, ventricular dyssynchrony, LBBB, RBBB, QRS, cGAN

# ABSTRAKT

Analýza ultravysokofrekvenčného EKG (UHF-ECG) poskytuje informácie o elektrickej komorovej dyssynchrónii. Okrem toho analýza UHF-ECG v reálnom čase umožňuje priamu optimalizáciu stimulačnej elektródy počas implantácie kardiostimulátora. V tejto diplomovej práci opisujeme poruchy komorového vedenia, súčasnú metódu analýzy UHF-ECG a hlavne predstavujeme niekoľko modelov hlbokého učenia na to, aby sme zistili, ktoré kroky UHF-ECG analýzy môžu byť hlbokým učením nahradené. Dáta použité na vývoj a validáciu modelov hlbokého učenia pochádzajú z 2 súkromných nemocníc (FNUSA-ICRC, Brno, Česko, FNKV Praha, Česko) a z 3 verejne dostupných databáz.

Najprv boli predstavené dve metódy hlbokého učenia na detekciu QRS komplexu a odhad trvania QRS komplexu v jednom kroku inferencie. Pri úlohe detekcie sme získali celkové F1-skóre 98,84 $\pm$ 0,51 % a pri úlohe odhadu trvania QRS komplexu strednú absolútnu chybu (MAE) 12,25 $\pm$ 2,16 ms. Táto metóda zvyšuje výkonnosť analýzy UHF-ECG a vďaka tomu môže výrazne skrátiť čas merania.

Okrem toho bol vyvinutý regresný model na odstraňovanie stimulačných impulzov založený na tzv. conditional generative adversarial networks. Výsledky boli vyhodnotené na základe korelácie 15 priemerných vysokofrekvenčných obálok v oblasti QRS komplexu medzi výstupom modelu a cieľovým signálom. Výsledky ukazujú vyššiu koreláciu na spontánnych signáloch a pokles korelácie so zvyšujúcim sa frekvenčným pásmom.

Napokon boli vytvorené dva modely konvolučených neurónových sietí (CNN) na odhad komorovej elektrickej dyssynchrónie (VED). Konkrétne CNN s vrstavmi v 1D a 2D. MAE medzi naším riešením a anotáciou je 12,61 $\pm$18,95 ms a 12,27 $\pm$17,73 ms pre 1D a 2D CNN. MAE na spontánnych signáloch je pre oba modely približne o 5 ms nižšia ako na stimulovaných údajoch, čo naznačuje potrebu odstrániť stimulačné impulzy.

Tieto modely hlbokého učenia prinášajú redukciu pipeline predspracovania a zároveň poskytujú výstup v jednom kroku inferencie. V prípade modelu detekcie QRS a odhadu trvania QRS je zlepšenie výkonu oproti súčasnému riešeniu evidentné a tieto kroky súčasnej analýzy UHF-ECG by mohli byť hlbokým učením nahradené. Avšak pre odstránenie stimulačných impulzov a odhad parametrov VED je potrebné zlepšiť výkon pre reálne použitie.



# KĽÚČOVÉ SLOVÁ

EKG, UHF-ECG, hlboké učenie, UNet, komorová dyssynchrónia, LBBB, RBBB, QRS, cGAN

# ROZŠÍRENÝ ABSTRAKT

Analýza ultravysokofrekvenčného EKG (UHF-ECG) poskytuje informácie o elektrickej komorovej dyssynchrónii. Klinický potenciál tejto metódy leží v zlepšení selekcie pacientov pre srdcovú resynchronizačnú terapiu. Okrem toho analýza UHF-ECG v reálnom čase umožňuje priamu optimalizáciu stimulačnej elektródy počas implantácie kardiostimulátora. V tejto diplomovej práci opisujeme poruchy elektrického komorového vedenia, súčasnú metódu analýzy UHF-ECG a hlavne vytvárame modely hlbokého učenia, ktoré by potenciálne mohli nahradiť jednotlivé časti UHF-ECG analýzy.

Na začiatku sú predstavené základy analýzy EKG na ktoré naväzuje časť o abnormalitách v sieňokomorovom vedení, tzv. atrioventrikulárnych (AV) blokoch. Ďalej sme sa presunuli na abnormality vo vedení komôr a to konkrétne blokádu ľavého a pravého Tawaroveho ramienka (LBBB a RBBB). Zaoberáme sa hlavne morfológiou EKG u týchto typov patológii a taktiež súčasnými možnosťami terapie. Ďalej bol predstavený súčasný stav analýzy UHF-ECG, ktorá umožňuje presnejšiu identifikáciu časovo priestorového rozloženia komorovej elektrickej depolarizácie a vyhodnotenia stupňa komorovej dyssynchrónie. Našou úlohou je implementovať hlboké učenie na jednotlivé časti analýzy UHF-ECG a zvážiť ich použiteľnosť.

Dáta použité na vývoj a validáciu modelov hlbokého učenia pochádzajú z 2 súkromných nemocníc (FNUSA-ICRC, Brno, Česko a FNKV Praha, Česko) a z 3 verejne dostupných databáz (Strict LBBB, CIPA, LUDB).

Prvý vytvorený model bol model pre detekciu QRS komplexov v UHF-ECG, ktorý bol následne rozšírený o estimáciu šírky QRS komplexu. Trvanie QRS komplexu je spolu s ejekčnou frakciou jedným zo základných parametrov pre selekciu pacientov pre srdcovú resynchronizačnú liečbu. Tento model teda poskytuje v jednom inferenčnom kroku informáciu o polohe QRS, jeho začiatku, konci a tým aj o jeho trvaní. Architektúra modelu je založená na architektúre segmentačného modelu konvolučnej neurónovej siete UNet. Všetky vrstvy modelu sú však pre účely spracovania signálu prevedené z 2D do 1D. Do modelu vstupuje okno signálu o dĺžke 3 s z 12 zvodov pri veľkosti vzorkovacej frekvencie 5,000 Hz. Vstup má teda veľkosť batch x 12 x 15,000 (3s x 5,000 Hz). Výstupom je vektor pravdepodobností výskytu QRS komplexu o rovnakej dĺžke ako vstupný signál, teda 3 s. Následne je výstup spracovaný na základe pravdepodobnostného a časového kritéria. Len tá časť signálu je považovaná za QRS komplex, kde je pravdepodobnosť QRS nad hodnotou 0.7 a tento segment má dĺžku aspoň 50 ms.

Dosiahnuté F1-score je 98.84 $\pm$ 0.51 % pre detekčnú úlohu a z hľadiska trvanie QRS komplexu je stredná absolútna chyba (MAE) rovná 12.25 $\pm$ 2.16 ms. Táto metóda zlepšuje presnosť súčasnej QRS detekcie zabudovanej vo VDI Vision softwari (F1 score 90 %) a tým by sa mohol signifikantne znížiť čas merania a hlavne čas operácie

počas implantácie kardiostimulátora.
Jedným zo základných krokov pre analýzu UHF-ECG, je odstránenie stimulačných pulzov u pacientov s kardiostimulátormi. Je to nevyhnutný krok pre zhlukovanie QRS na základe morfologickej skupiny. Odstránenie vzostupnej hrany stimulačného impulzu je jednoduchá úloha avšak odstránenie fázy po dobíjaní stimulátora je náročné, kvôli jej nízkej amplitúde.
Pre túto úlohu boli využité data z FNUSA pre tréning a válidáciu a data z FNKV pre nezávislý test. Ako model hlbokého učenia bola aplikovaná architektúra pix2pix ktorá patrí do triedy modelov nazývaných conditional Generative Adversarial Networks (cGAN). Tento model pri tréningu využíva tzv. generátor (architektúra UNet), ktorý na svojom výstupe poskytuje signál s odstránenými stimulačnými pulzami a diskriminátor, čo je bežný klasifikátor, ktorý núti generátor približovať sa k skutočnosti (k anotácii, čo je signál, kde sú stimulačné impulzy detekované a odstránené na základe lineárnej funkcie doplnenej splinom). Vstup do modelu je 0.2 sekundové okno derivovaného signálu. Počas tréningu do modelu okrem stimulavných dát vstupujú aj spontánne data, ktoré buď ostávajú spontánne alebo sú v nich umelo vytvorené stimulačné pulzy. Počet, trvanie, ampliúda a polarita týchto umelo vytvorených stimulačných impulzov je náhodná.
Po natrénovaní modelu je ďalej využívaná len architektúra generátora. Výstup a anotácia modelu sú derivované signály, ktoré je pre ďalšiu analýzu nutné integrovať. Keďže UHF-ECG analýza je vykonávaná na amplitúdových obálkach v oblasti QRS komplexov, tak pre analýzu výsledkov metódy boli vytvorené priemerné vysokofrekvenčné amplitúdové obálky v oblasti QRS komplexu v 15 frekvenčných pásmach z výstupu modelu a z anotácie. Vytvorené obálky boli porovnané na základe Spearmanovej korelácie. Bolo zistené, že u spontánnych signálov, kde nie je nutnosť odstraňovať stimulačné pulzy je korelácia anotácie a výstupu vyššia a má menšie konfidenčné intervaly narozdiel od stimulovaných signálov. Taktiež so zvyšujúcim sa frekvenčným pásmom dochádza k znižovaniu korelácie u spontánnych aj stimulovaných dát.
Výhoda oproti súčasnej metóde aplikovanej vo VDI Vision softwari leží v odstránení stimulačných impulzov v jednom inferenčnom kroku bez potreby predošlej detekcie QRS. Avšak ak sa pozrieme na výsledky korelácie amplitúdových obálok v rôznych frekvenčných pásmach, na to, aby mohol byť model použitý v praxi je nutné dostať výkonnosť modelu na stimulovaných datach aspoň na úroveň výkonnosti na spontánnych.
Na záver boli vytvorené 2 modely pre estimáciu hodnoty komorovej elektrickej dyssynchrónie (VED). Keďže 1/3 pacientov s LBBB morfológiou, redukovanou ejekčnou frakciou (menšia alebo rovná ako 35 %) a s trvaním QRS nad 150 ms neodpovedá na CRT, bola v minulosti vytvorená technika pre získavanie hodnoty komorovej

elektrickej dyssynchrónie. Táto hodnota reflektuje elektrickú dyssynchróniu medzi pravým komorovým septom a laterálnou stenou ľavej komory.
Pre tréning, validáciu a testovanie modelov pre estimáciu VED boli využité data z FNUSA a FNKV nemocnice. V tomto prípade boli data zmiešané tak, aby sa rovnaký pacient nenachádzal medzi rozdeleniami. Data boli zmixované hlavne z dôvodu rôzneho typu patológii u pacientov v daných nemnocniciach. Vo FNUSA sa nachádzajú hlavne pacienti s LBBB morfológiou a vo FNKV hlavne pacienti s AV blokádami. Vstupom do oboch vytvorených modelov je 8 sekundové okno derivovaného signálu zo 6 hrudných zvodov (V1-V6) a výstupom je konkrétna hodnota VED bez nutnosti ďalšieho spracovávania.
Pre estimáciu VED boli vytvorené 2 modely: 1D a 2D konvolučná neurónová sieť. Nápad za použitím 2D varianty pramenil z toho, že parameter VED sa pôvodne odhaduje zo 6 hrudných zvodov súčasne v čase a sleduje sa časový posun medzi QRS komplexom vo zvodoch V1 až V6, preto aplikujeme 2D konvolúciu, aby sieť mohla vidieť viacero zvodov súčasne v čase. Táto teória však nebola potvrdená, keďže oba modely vedú k podobným výsledkom. Úspešnosť nášho modelu je meraná na základe MAE medzi anotovaným a estimovaným VED parametrom u testovacej sady dát. MAE pre 1D model je 12.61 $\pm$18.95 ms a pre 2D CNN je to 12.27 $\pm$17.73 ms. Oba modely dosahujú vyššiu úspešnosť na spontánnych ako na stimulovaných datach, čo naznačuje nutnosť odstraňovania stimulačných pulzov. Taktiež, oba modely majú lepšiu úspešnosť na kladných hodnotách VED a to z dôvodu rozloženia dát v trénovacej sade (len 35 % signálov s negatívnou hodnotou VED). Na záver boli vytvorené korelačné diagramy s príslušnou Spearmanovou koreláciou. 2D varianta modelu dosahovala vyššiu koreláciu v porovnaní s 1D variantou (0.85 vs. 0.83) a to hlavne u stimulovaných signálov (0.81 vs. 0.77).
Keďže iné metódy ktoré merajú elektrickú dyssynchróniu neexistujú, tak sme našu metódu porovnali s metódou merania mechanickej dyssynchrónie komôr, ktorá sa meria pomocou echokardiografie. Naša metóda má skrz pevnú architektúru a nastavené parametre perfektnú reproducibilitu narozdiel od ľudského pozorovateľa pri meraní mechanickej dyssynchrónie (intra reproducibilita v 95 % konfidenčnom intervale je -27-26 ms). Výsledky naznačujú, že naše modely dokážu odhadnúť VED pre spontánne data, ale výkonnosť u stimulovaných dat musí byť pre reálne použitie vylepšená.
Výhodou všetkých týchto modelov je minimálne predspracovanie signálu a poskytnutie požadovaného výstupu v jednom kroku inferencie. Ale zatiaľ čo prezentované metódy fungujú perfektne v prípade detekcie a segmentácie QRS, identifikovali sme aj slabé miesta v metódach odstraňovania stimulačných pulzov a odhadu VED. Avšak, všetky tieto pozorovania sú nevyhnutné pre ďalší vývoj analýzy a pomáhajú určiť, ktoré časti analázy UHF-ECG by mohli byť nahradené hlbokým učením.

KOŠČOVÁ, Zuzana. *Analysis of ultra-high frequency ECG using deep learning*. Brno: Brno University of Technology, Faculty of Electrical Engineering and Communication, Department of Biomedical Engineering, 2023, 68 p. Master's Thesis. Advised by Ing. Filip Plešinger, Ph.D.

# Author's Declaration

| | |
|---|---|
| **Author:** | Bc. Zuzana Koščová |
| **Author's ID:** | 203197 |
| **Paper type:** | Master's Thesis |
| **Academic year:** | 2022/23 |
| **Topic:** | Analysis of ultra-high frequency ECG using deep learning |

I declare that I have written this paper independently, under the guidance of the advisor and using exclusively the technical references and other sources of information cited in the paper and listed in the comprehensive bibliography at the end of the paper.

As the author, I furthermore declare that, with respect to the creation of this paper, I have not infringed any copyright or violated anyone's personal and/or ownership rights. In this context, I am fully aware of the consequences of breaking Regulation § 11 of the Copyright Act No. 121/2000 Coll. of the Czech Republic, as amended, and of any breach of rights related to intellectual property or introduced within amendments to relevant Acts such as the Intellectual Property Act or the Criminal Code, Act No. 40/2009 Coll. of the Czech Republic, Section 2, Head VI, Part 4.

Brno ..... .....

author's signature*

*The author signs only in the printed version.

# ACKNOWLEDGEMENT

I would like to thank my thesis supervisor Ing. Filip Plešinger Ph.D., colleague Ing. Radovan Smíšek and whole Medical Signals department of ISI Brno of CAS for their consultation, support and valuable advices.

# Contents

# List of Figures

# List of Tables

# Introduction

According to the WHO, heart disease is the number one killer in the world responsible for 32% of deaths in 2019 [1]. Heart activity is usually observed using electrocardiography (ECG) which is one of the fundamental examination methods in cardiology to analyze heart disorders. The first part of this work focuses mainly on ventricular conduction abnormalities and the therapeutic options for these disorders.

Under normal circumstances in a healthy heart, both ventricles are depolarized simultaneously. These contractions could, however, occasionally become dyssynchronized, which is characteristic of the Left or Right Bundle Branch Block.

To examine the electrical dyssynchrony of the ventricles, an Ultra-high-frequency ECG (UHF-ECG) technique has been developed [2]. UHF-ECG analysis results may help to select patients for Cardiac Resynchronization Therapy (CRT) [3] and could be also used for the optimization of pacing electrode location in real-time during pacemaker implantation. However, the current method for UHF-ECG analysis is computationally intensive and time-consuming [4]. Therefore, to improve real-time UHF-ECG analysis, it is beneficial to reduce the preprocessing pipeline. In recent years, a number of high-impact studies using deep learning to analyze and classify ECGs in large patient cohorts were published. In the second part of this work, we propose deep learning models for individual steps of UHF-ECG analysis which could not only speed up the analysis but also improve its performance. Generally speaking, our goal is to see if certain parts of the UHF-ECG analysis could be replaced by deep learning.

This master thesis is organized as follows: The first chapter describes the heart conduction system, which is followed by the second chapter dealing with the ECG analysis. The following chapters describe atrioventricular and ventricular conduction abnormalities. Chapter 5 describes the current methods for UHF-ECG analysis and chapter 6 focuses on deep learning as an option for improving UHF-ECG analysis. The 4 following chapters focus on specific real-time deep learning methods used for UHF-ECG analysis, namely, detection of QRS complexes, QRS duration estimation, pacing stimuli removal and assessment of ventricular electrical dyssynchrony. At the beginning of each of these chapters there is a description of the used datasets and applied methods. Then the results are summarized and discussed along with the contribution of the above models in relation to the current state of the UHF-ECG analysis in the separate discussions. The images in this work were created using BioRender [5] and Adobe Illustrator. The program codes for this work are not freely available, but they are available for viewing on request from me or thesis supervisor.

# 1 Electrophysiology of the heart

The heart is a four-part muscular pump driving the circulation of blood (Fig. 1.1). It has an internal pacemaker and does not need nerve stimulation to function normally, despite being under the influence of the autonomic nervous system. A cardiac conduction system is a system of specialized muscle cells in the heart that carry an electrical charge (potential) and are thus adapted to generate cardiac impulses and conduct them through the heart's compartments [6].

In a case of a normal heartbeat, the electrical activity starts at the sinoatrial (SA) node of the right atrium and continues down throughout the ventricles of the heart. As a wave of depolarization travels through the heart, it causes contraction of the myocardium. Depolarization might be considered as an advancing wave of positive charges within the heart's myocytes [7].

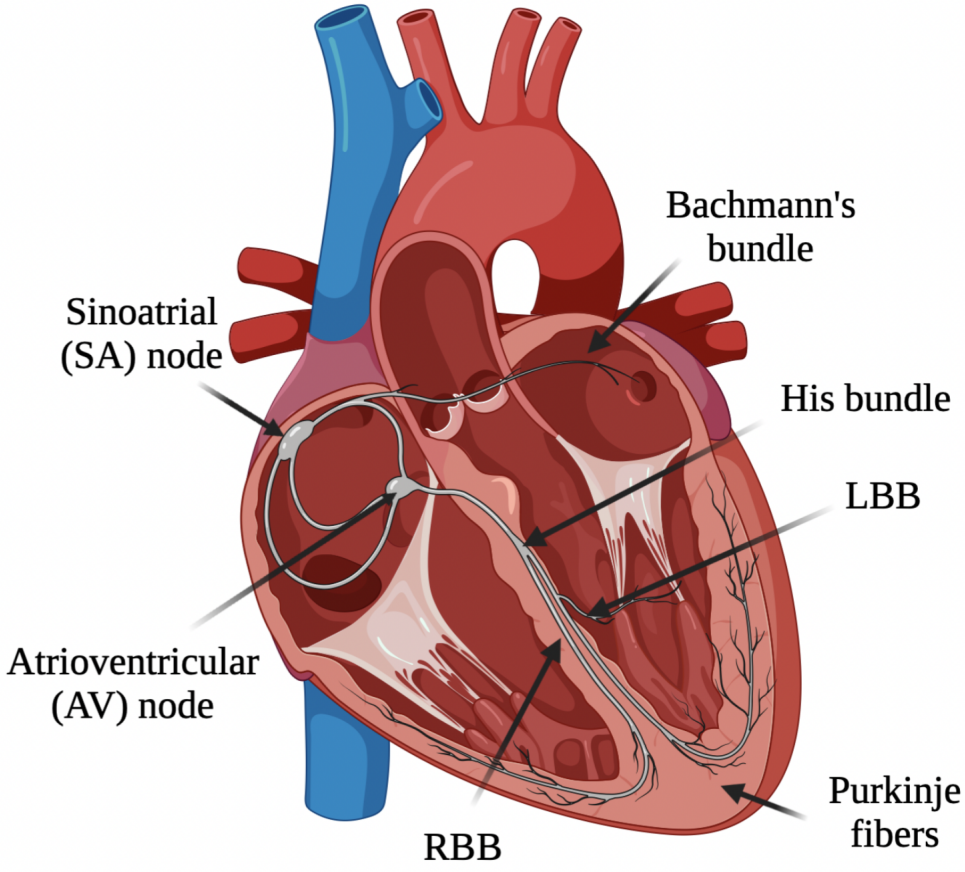


Fig. 1.1: Conduction system pathways, RBB, and LBB refer to the right and left bundle branches, respectively.

Depolarization initiates from the sinoatrial (SA) node, which is located in the upper posterior wall of the right atrium. It is a heart dominant pacemaker and it

is comprised of a unique group of cells that undergoes automaticity. The pacing activity of the SA node is called a Sinus rhythm. As the SA node depolarizes, an electrical signal proceeds from the SA node. Depolarization wave is simultaneously transmitted to the right atrium via a bundle of cells called Bachman's Bundle [7, 8].

Depolarization then continues to the atrioventricular (AV) node which is located further inferior in the right atrium by the interatrial septum. The AV node conducts the depolarization very slowly, thus causing a desirable pause in atrioventricular conduction - atrial contraction (depolarization) must be completed first, followed by ventricular contraction (depolarization). If this delay did not occur, the atria and ventricles would contract simultaneously, and blood would not flow appropriately through the heart. In the case of damage to the SA node, the AV node takes over the role of the pacemaker - it is also referred to as a secondary pacemaker [7, 9].

Atrioventricular valves prevent blood backflow to the atria and electrically insulate the ventricles from the atria. Depolarization can only reach the ventricles from the atria via His bundle, which is connected to the AV node. His bundle, located inferior to the AV node in the interventricular septum, transmits the conduction down to the left and right bundle branches and their subdivisions. The His Bundle and both right and left bundle branches are bundles of rapidly conducting Purkinje fibers. The terminal branches of the Purkinje fibers distribute ventricular space with the electrical output. The terminal filaments of the Purkinje fibers span beneath the endocardium that lines both ventricular cavities, therefore myocytes depolarization of the ventricles begins at the lining and continues arcing toward the epicardium (outside surface) [9, 10].

# 2 ECG analysis

Electrocardiography (ECG) is a fundamental diagnostic method in cardiology. ECG records the electrical activity of the heart providing valuable information about heart function and structure. The standard ECG is a non-invasive examination where electrodes placed on the skin are used to measure the voltage difference as a result of the propagation of the excitation wave through the myocardium. During depolarization and repolarization, myocardial fibers become a source of voltage changes that can be measured from the body surface. The stimulating wave of depolarization makes the interiors of the myocytes positive and stimulates them to contract. Then the myocyte interiors regain their resting negative charge during the repolarization phase that follows [11].

According to the position of the electrodes, the electrodes are differentiated into the limb and precordial electrodes. In clinical practice, a 12-lead ECG recording is standardly used (Fig. 2.1). It consists of three limb bipolar leads (I, II, III), three limb unipolar leads (aVR, aVL, aVF) formed by connecting each limb electrode to the Wilson central terminal, and six unipolar precordial leads (V1-V6).

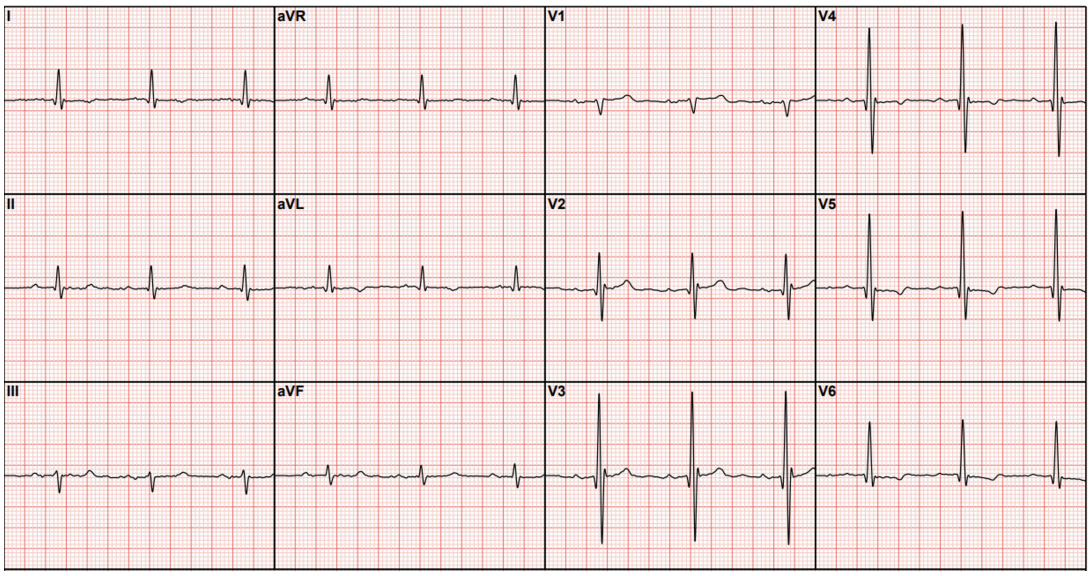


Fig. 2.1: Example of a standard 12-lead ECG [12].

A graphical record of the electrical activity of the heart over time is called an electrocardiogram. The propagation of depolarization through the myocardium is displayed differently with respect to the lead, depending on the direction and plane in which it is positioned relative to the heart. The potential propagation path in the heart has a typical character and thus produces typical deflections - waves, oscillations, and lines that correspond to a particular phase of the electrical cardiac

cycle (Fig. 2.2).

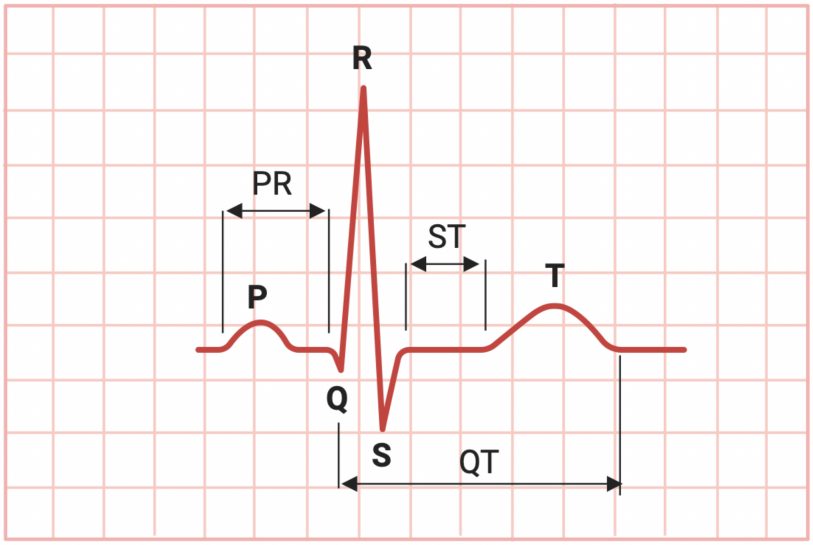


Fig. 2.2: ECG of the heart in normal sinus rhythm with marked waves, intervals, and segments that correspond to a particular phase of the electrical cardiac cycle. The P wave represents atrial depolarization, the QRS complex points to ventricular depolarization, and T wave indicates ventricular repolarization. PR segment is the segment between the end of the P wave and the beginning of the QRS complex, the ST segment connects the QRS complex and the T wave, and the time from the start of the Q wave to the end of the T wave is called QT interval.

The depolarising wave originating in the SA node propagates to the atrial muscles, which are depolarised, and this appears as a P wave on the ECG recording (Fig. 2.3 a.). Slow conduction in the atrioventricular node slows the progression of depolarization from the atria to the ventricles and separates atrial from ventricular systole. On the ECG, this corresponds to an isoelectric line (Fig. 2.3 b.). The total transfer of depolarization from the atria to the ventricles is indicated by the PQ interval [7, 11].

This is followed by depolarization of the ventricles, forming a QRS complex on the ECG recording (Fig. 2.3 c.). The excitation progresses through His bundle to the musculature of the interventricular septum, where the depolarization spreads from left to right. The ECG shows either a negative Q oscillation or a positive R oscillation, depending on the lead. The next progression of excitation spreads to the apex, forming the middle part of the QRS complex, in most leads the oscillation of R. From there the depolarization spreads through the Purkinje fibers to both ventricles, from the endocardium to the epicardium, completing the ventricular QRS complex with the S wave. QRS complex overlaps with atrial repolarization.

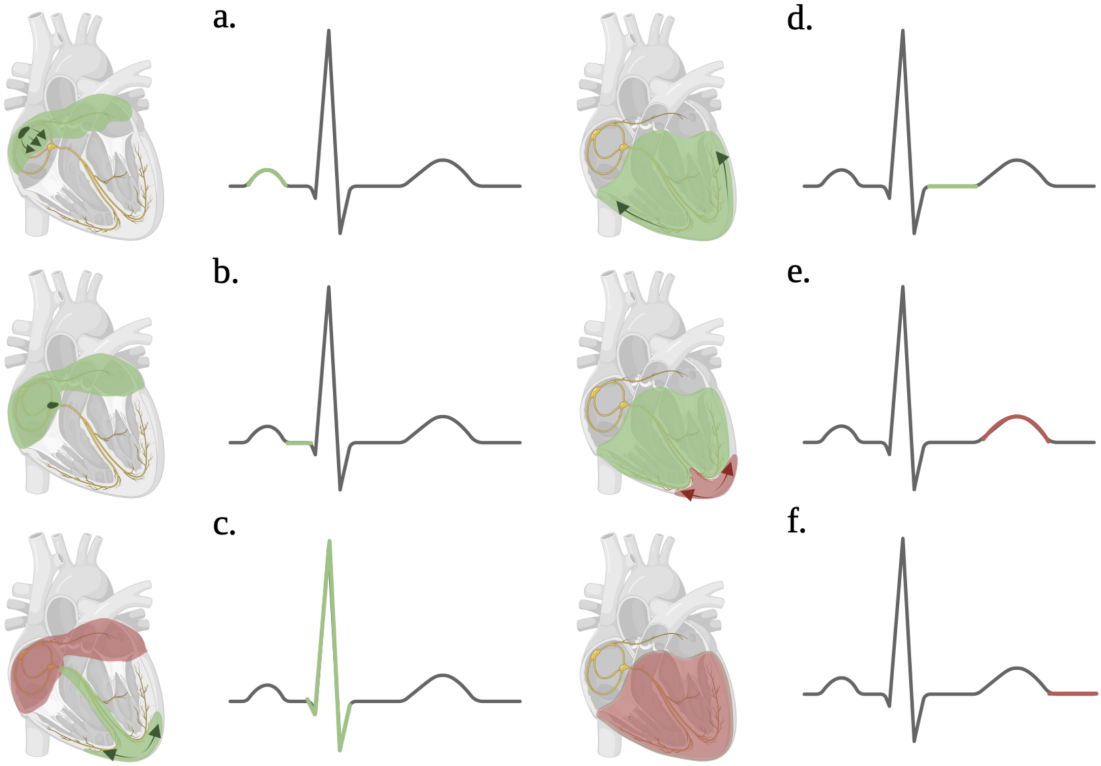


Fig. 2.3: A graphical record of the electrical activity of the heart, a. atrial repolarization originating from the SA node, b. complete atrial depolarization with a desirable pause in the AV node, c. atrial repolarization, and beginning of ventricular depolarization, d. complete ventricular depolarization, e. beginning of ventricular repolarization, f. complete ventricular repolarization.

After the depolarization is over, the electrical activity of the heart is momentarily zero, the muscle fibers are in the plateau phase when no electrical currents propagate through the myocardium. It appears as an isoelectric line on the ECG recording - the ST segment (Fig. 2.3 d.). After this point, ventricular repolarization begins and proceeds in the opposite direction from the epicardium to the endocardium. Thus, a T wave is generated (Fig. 2.3 e. and f.) [7, 11].

The evaluation of ECG recordings allows us to detect arrhythmias caused by defects in the generation or conduction of impulses. It also plays an important role in detecting ischemic changes, localization, and stage of myocardial infarction. Changes on the ECG are found either in all leads or in one or a group of leads that are related to each other due to the anatomy of the heart.

# 3 Atrioventricular conduction abnormalities

Blocks in any part of the heart conduction system slow or prevent the conduction of electrical impulses. They may originate in the SA node, AV node, or in the larger divisions of the ventricular conduction system. In this chapter, we will discuss the blocks that originate from the atrioventricular node. AV blocks either delay or eliminate conduction from the atria to the ventricles. The brief interval between atrial and ventricular depolarization is prolonged by minor AV blockages, most of the AV blocks prevent some or all supraventricular impulses from reaching the ventricles [7].

## 3.1 First degree AV block

When the PR interval is longer than 0.2 s (usually 0.21 - 0.4 s but may be as long as 0.8 s) in every cycle and the P-QRS-T sequence is standard in every cycle as well, the 1°AV block is present. A QRS complex follows each P wave. Note that the PR interval represents the time from the onset of atrial depolarization to the onset of ventricular repolarization. It does not reflect the conduction of the stimuli from the sinus node to the atrial space. Therefore, prolonged PR interval with narrow QRS reflects a block in the AV node. If the widened QRS complex is observed, it points to a blockage in the lower parts of the heart conduction system; His bundle or Purkinje fibers. Although, prolonged PR interval with widened QRS can also mean disruption in the AV node together with blockage in one of the bundle branches (or both) [7, 13].

1°AV block can occur in healthy individuals, or athletes, or can be drug-related. Diagnoses associated with 1 °AV block include myocarditis[1], congenital heart disease[2] or rheumatic heart disase[3] [13].

## 3.2 Second degree AV block

In second degree AV block, some depolarizations are conducted from the AV node to the ventricles, while other atrial depolarizations are completely inhibited leaving lone P waves without an accompanying QRS complex, thus without ventricular depolarization. There are two types of 2°AV blocks: Wenckebach and Mobitz [7].

[1]Myocarditis stands for inflammation of myocardium

[2]CHD is a range of birth defects that affect the normal way the heart works

[3]RHD is a condition in which the heart valves have been permanently damaged by inflammatory disease

Wenckebach 2°AV block originates from the AV node. On an ECG, the PR interval progressively increases with each cycle until the final P wave of the series does not reach the ventricles and therefore is not followed by the QRS complex. This series can be observed repeatedly. The typical Wenckebach series contains anywhere from 2-8 cycles (P: QRS ratio; 2:1, 3:2, 4:3, etc.) [7].

In the case of Mobitz 2°AV block, the number of atrial depolarizations is completely blocked before conduction to the ventricles is successful. More P waves are generated in relation to successful QRS complexes, with a ratio of 2:1, 3:1, or more. This series occurs repeatedly. Exceedingly slow ventricular rates may result in consciousness loss (syncope). Every cycle with Mobitz that has a missing QRS has a regular, punctual P wave. Regular sinus or atrial rhythm with intermittent nonconducted P waves, with no sign of atrial prematurity, can be observed. For the conducted beats PR interval is constant.

To distinguish between Wenckenbach and Mobitz 2°AV block in a 2:1 (P: QRS) series, it is necessary to look at the duration of the QRS complex in addition to the duration of the PR interval. Because for 2 P waves, we are not able to detect a progressive prolongation of the P wave which is observable in the Weckenbach type and not present in the Mobitz type. Wenckebach frequently originates in the AV node, hence AV series 2:1 of this origin often has an initial lengthened PR interval with no wide QRS pattern [7, 13]. The His Bundle, which is typically where Mobitz begins, lies underneath the AV node, thus we can see that it frequently has a normal PR with a broadened QRS pattern (in 80% of cases) in a ratio 2:1 (P waves: QRS complex). Other mechanisms for the distinction between the 2 types include the response to increasing heart rate and AV conduction, where improvement occurs with Wenckebach and worsening occurs with the Mobitz type. In contrast, with maneuvers lowering heart rate and AV conduction, Wenckebach block worsens and Mobitz block improves [13].

In addition to the diagnosis that occurs in the case of the 1°AV block, the etiology of the 2°AV block may also be myocardial infarction (inferior for Wenckebach, anterior for Mobitz type) [7].

## 3.3 Third degree AV block

3°AV block prevents conduction of sinus-paced atrial depolarizations from reaching the ventricular tissue. Atrial and ventricular rhythms are independent of one another because atrial impulses consistently fail to reach the ventricles. Below the complete block, there is an automaticity focus pacing the ventricles at their inherent rate. The location of the automaticity focus depends on the location of the complete block [7].

One possible location is the occurrence of a complete AV block at the upper part of the AV node, which allows the junctional focus to escape and stimulate the ventricles. PP and RR intervals are constant, but PR intervals vary. This is because the rhythm of the atria remains independent of the rhythm of the ventricles. The atria are stimulated by the SA node, but ventricles are independently paced by junctional focus with idiojunctional rhythm. The ventricular rate ranges from about 40 to 60 beats per minute and is usually slower than the atrial rate. QRSs are usually normal (narrow) [7, 13].

Sometimes the block's location is in the lower part of the AV node or even in the His bundle leaving only a ventricular focus to pace without junctional focus available. Ventricular focus paces the ventricles at their inherent slow rate of only 20 to 40 beats per minute. Cerebral blood flow might be compromised resulting in syncope (Stokes-Adams Syndrome). In order to recognize ventricular focus it is necessary to note the morphology and duration of the QRS complex. In this case, we observe wide QRS complexes with premature ventricular contraction morphology. Complete AV block patients require ongoing monitoring, airway maintenance, and eventually, an artificial pacemaker [7, 13].

Complete heart block may result from myocardial infarction (MI), which accounts for 5–15% of all myocardial infarctions. First-degree AV block or Wenckebach 2°AV block is frequently present before inferior MI. Complete heart block, which often precedes Mobitz 2°AV block or bifascicular block develops in anterior MI as a result of severe damage to the left ventricle and is associated with death rates as high as 70%. Other causes might include degenerative heart disease, infiltrative disease, or endocarditis in which conduction failure and complete heart block are caused by inflammation or edema of the septum and peri-AV nodal tissues [13].

# 4 Intraventricular conduction abnormalities

## 4.1 Bundle branch blocks

Under normal circumstances in a healthy heart, the depolarization stimulus is quickly conducted from His bundle by the right and by the left bundle branches to the right and left ventricles. Ordinarily, both ventricles are depolarized simultaneously. The electrical activation of the right and left ventricle from their branches results in the QRS complex, which then represents the sum of two parallel but independent electrical phenomena [7, 14].

A block in one of the bundle branches is a condition in which there is a delay or blockage along the pathway that electrical impulses travel to make the heartbeat. With bundle branch block (BBB), the unblocked branch conducts depolarization regularly, while in the block bundle branch depolarization needs to pass through surrounding tissue, which causes slower conduction than in the bundle branch which is specialized for this task. After the blocked part, depolarization proceeds at a normal pace again. Therefore, in a BBB if the conduction in His bundle is normal and one bundle branch is blocked, the corresponding ventricle is depolarized slightly later than the other one, which causes two joined QRSs to appear on an ECG as widened QRS, which means the increasing duration of the QRS complex with unchanged PR interval. The frequency of bundle branch block in the young population ranges from 0.1 - 0.3%. While in elderly healthy subjects it ranges from 0.7 -2% [15, 13].

### 4.1.1 Right bundle branch block

In the right bundle branch block (RBBB) activation of the right ventricle is delayed, as depolarisation originates from the left ventricle across the septum. Therefore, in the doubled QRS, the first R wave is represented by a left punctual ventricle and the second R wave is represented by the depolarization of a delayed right ventricle. This is mostly visible on chest leads V1 and V2 (Fig. 4.1). RBBB has two variants, complete and incomplete blockage. In complete blockage, the right bundle branch is completely disrupted and the impulse reaches both ventricles only via the LBB and then passes from the left ventricle through the myocardium to the right ventricle.

In the complete RBBB, a prolonged QRS complex may be observed on the ECG ($\geq$ 120 ms) together with a secondary R' wave in precordial leads V1 and V2 with the second R' wave usually having higher amplitude than the initial R wave. Delayed onset of intrinsecoid deflection[1] ($>$ 50ms) in V1 and V2 leads is likely to occur. In

[1]Intrinsecoid deflection time is measured from the beginning of the QRS complex to the peak of the R wave

leads V1 and V2 there may be present ST and T wave changes like T wave inversion and downsloping ST segment. Wide slurred S waves in lead I, V5, and V6 are observed [13].

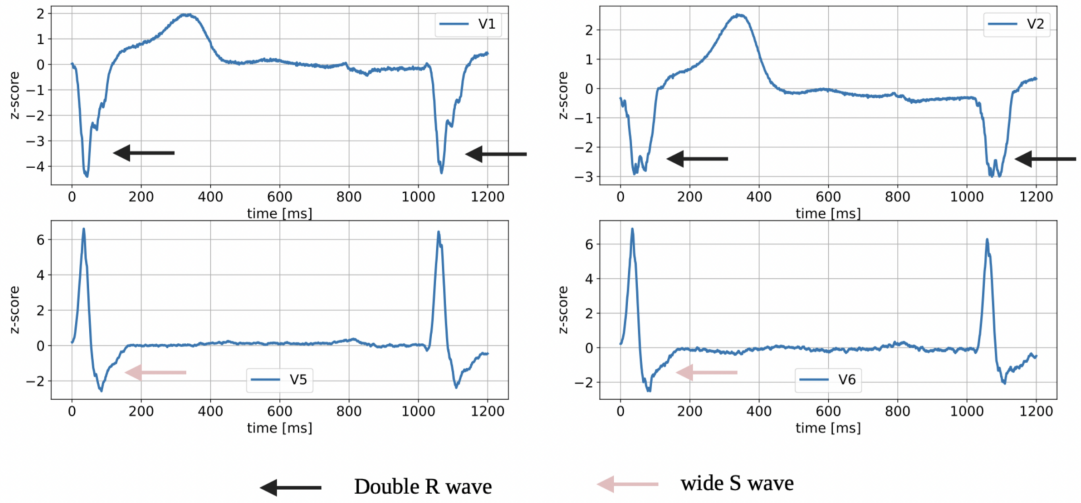


Fig. 4.1: RBBB with marked characteristics on an ECG. Secondary R' (double R) wave in precordial leads V1 and V2 could be observed together with wide S wave in V5 and V6 leads.

In incomplete blockage the right bundle branch is not completely disrupted, it still conducts the depolarizing impulse but more slowly. This is the main difference between complete and incomplete blockage. In incomplete blockage, the QRSd is $<$ 0.12 ms [13].

RBBB occurs in normal healthy individuals, with no previous records of structural heart disease at a prevalence of 0.2%. The prognosis for these patients is essentially the same as for the general public. However, RBBB is linked to a double increase in mortality among individuals with coronary artery disease when compared to patients without BBB. RBBB may not cover up the signs of an inferior infarction. Still, an anterior infarction may be difficult to detect in RBBB. On the other hand, RBBB does not affect ST segments, and if elevations are present in a patient with suspected infarction, these are likely to be clinically significant changes [13]. Right bundle branch block is further associated with hypertensive heart disease, myocarditis, dilated cardiomyopathy (DCM)[2], rheumatic heart disease (RHD), degenerative disease of the conduction system, pulmonary embolism (PE) [3] or cor pulmonale [4]. ST segment depression associated with RBBB indicates ischemia [15, 13].

[2]DCM causes the heart to expand and become inefficient at pumping blood

[3]PE is a disease in which blood flow from the heart to the lungs is partially or completely blocked

[4]Cor pulmonale is right ventricular dilatation resulting from acute or chronic pre-capillary

Usually, a right bundle branch block does not cause any symptoms by itself. If there are additional issues in addition to the right bundle branch obstruction, symptoms are more likely to occur.

### Treatment of RBBB

Generally, isolated RBBB without any other cardiac disorders, if occurring in a healthy population, requires no further treatment. If RBBB occurs in patients with heart failure with a low ventricular ejection fraction (EF) [5], cardiac resynchronization therapy (CRT) is to be considered. CRT is a procedure that involves implanting electrodes into the right (usually the apex) and left ventricles (usually the coronary sinus) of the heart. This procedure is used to treat heart failure by synchronizing the left and right ventricles using a pacemaker. Since the introduction of CRT for patients with heart failure, an increasing number of patients undergoing CRT had QRS morphology with RBBB. This is because, in the beginning, the only ECG marker for CRT was QRS duration. However, past observational studies that assessed the effect of CRT show excess mortality in RBBB CRT-treated patients compared to LBBB CRT-treated patients. Consequently, it was advised against using CRT in patients with typical RBBB morphology [16].

Nevertheless, some patients with heart failure and an RBBB pattern on their ECG also have a concurrent superimposed delay in left ventricular activation. In wider QRS, RBBB frequently masks the underlying co-existing LBBB. Atypical RBBB patterns include broad, slurred, occasionally bifid R waves on leads I and aVL and a leftward axis deviation that is typically seen in patients with LBBB QRS morphology. Acute response to CRT is clinically significant and has favorable values, according to a recent assessment of various studies that took CRT into account in the subset with atypical RBBB [17].

CRT is recommended in symptomatic patients with heart failure and sinus rhythm with EF of left ventricle lower or equal to 35%, QRSd $>$ 150 ms, and non-LBBB QRS morphology (including atypical RBBB). The goal is to improve symptoms and reduce morbidity and mortality [18].

If the conditions are the same as in the paragraph above with a difference in QRSd (130 - 149 ms), patients belonging to the New York Heart Association (NYHA) class IV[6] may be considered for CRT [18].

---

pulmonary hypertension

[5]EF measures the amount of blood the left ventricle pumps out to your body with each contraction

[6]IV - Unable to carry out any physical activity without discomfort

### 4.1.2 Left bundle branch block

The left bundle-branch block (LBBB) completely modifies the electrical activation of the left ventricle and QRS complex on ECG. Interventricular septum activation, which in physiologic settings is left-sided, starts on the right side of the structure. The electrical impulse then spreads inferiorly, to the left, and slightly anteriorly [14]. As a result, the left ventricle experiences a nonhomogeneous and delayed depolarization that can only be partially retained in the presence of a functional distal left bundle branch and Purkinje network. In the left bundle branch block, the right ventricle is depolarized on time, therefore a double R wave occurs in the lateral leads V5 and V6. The first R wave represents depolarization of the right ventricle and the second R wave in the widened QRS is caused by the delayed depolarization of the left ventricle. Similarly to the RBBB, LBBB has two variants, complete and incomplete blockage. In complete LBBB, the impulse that comes from the atria activates the ventricles only through the RBB, and then the impulse travels through the myocardium to the left ventricle and depolarizes it.

For a complete LBBB (Fig. 4.2), the ECG shows prolonged QRS complexes (>120 ms), and increased intrinsecoid deflection time (80–120 ms), because of delayed intincsecoid onset (>50ms) [13]. Furthermore, it shows rS or QS complexes in V1–V2 [14], broad monophasic R waves in I, V5, and V6 that are usually notched or slurred and loss or significant reduction of septal Q wave in lateral leads I and aVL. Leads I and aVL typically display a negative ST-T pattern [14, 15]. It also shows ST depression and T wave inversion in I, V5, and V6. ST elevation can be seen in an upright T wave in leads V1 and V2 [13].

In an incomplete LBBB, the left bundle branch is damaged but not completely blocked. It conducts the pulse more slowly. The only difference in the ECG compared to the complete block is the width of the QRS complex, which in this case lasts from 0.09-0.12 ms [13].

LBBB can be seen in patients with left ventricular hypertrophy (LVH)[7]. According to pathological and echocardiographic studies, 80% of patients with LBBB have abnormally enlarged LV mass, however, a formal diagnosis of LVH should not be established in the context of LBBB [13]. LBBB can be caused also by myocardial infarction and ischemic heart disease (IHD)[8]. In the presence of LBBB, no infarction changes can be observed on the ECG. This does not mean that the ECG is worthless. If a patient hospitalized with chest pain with suspected ischemia shows a newly developed LBBB on the ECG, an infarction is very likely and appropriate treatment

[7]LVH is characterized by an increase in left ventricular mass caused by an increase in wall thickness, an expansion of the left ventricular mass, or a combination of the two

[8]IHD is defined as inadequate blood supply to a local area due to blockage of the blood vessels supplying the area

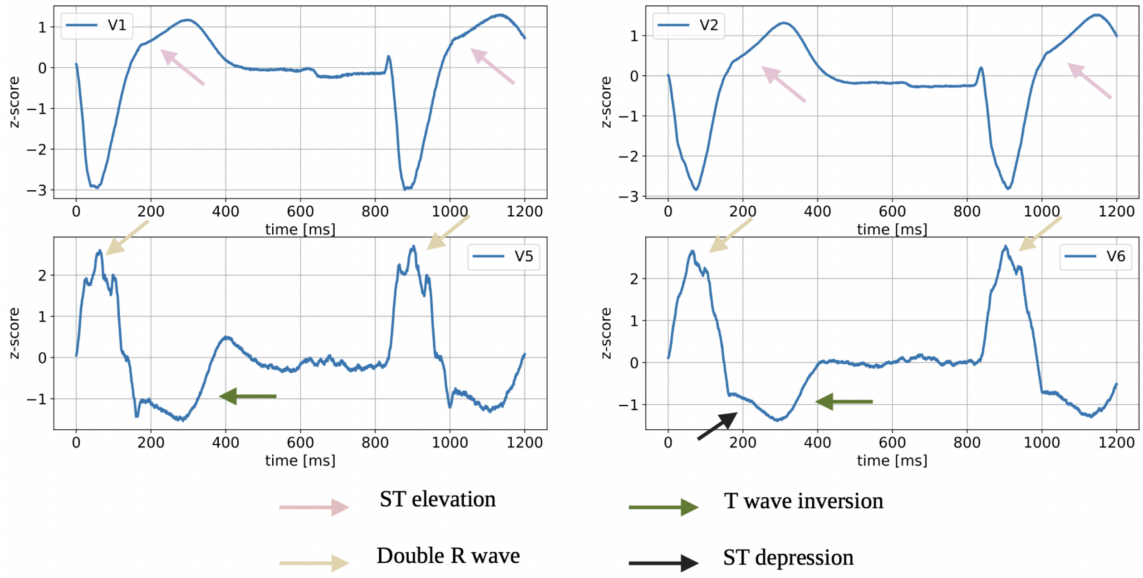


Fig. 4.2: LBBB with marked characteristics on an ECG. ST elevation in leads V1 and V2 can be observed, together with ST depression, T wave inversion and double R wave in V5 and V6.

should be initiated [15]. Furthermore, LBBB is often associated with degenerative disease of the conduction system, dilated cardiomyopathy (DCM), congenital heart defects (CHD), or arterial hypertension. Rarely, it also occurs in healthy people without any heart disorders [15, 13].

About 0.06% to 0.1% of the overall population suffers from LBBB. LBBB is seen in about 33% of heart failure patients. Other than the distinctive ECG pattern, LBBB is asymptomatic; there are no other signs or symptoms. The presence of LBBB without other signs of heart disease is accompanied by approximately a 30% increase in the risk of death compared with persons with a normal ECG. The risk of death is further doubled if LBBB suddenly develops in a person who previously had a normal ECG, even if the person is asymptomatic [15].

### Treatment of LBBB

If a patient is diagnosed with LBBB but is asymptomatic, they may not need treatment for LBBB but for other diagnoses associated with LBBB (e.g. high blood pressure). Another treatment option is CRT, in which it is necessary to follow guidelines [18]. Considering the inclusion criteria of large randomized clinical studies (RCS) focused on CRT, according to the NYHA in class II-IV[9], where QRS duration >

[9]II - Slight limitation of physical activity

130 ms and EF < 35-40%, it is estimated that 15-30% of patients with heart failure reduced ejection fraction (HFrEF) may benefit from CRT [18]. The most beneficial effect on morbidity and mortality, according to the RCS results, was shown in the groups of patients with EF 35% or less, who had a dominant sinus rhythm with LBBB and were in NYHA functional class II-IV. In other patient groups, female sex with QRSd >150 ms and prolonged PR interval appeared as factors with a tendency to better outcome [18].

CRT is recommended in symptomatic patients with heart failure (HF) and sinus rhythm with EF of the left ventricle (LVEF) lower or equal to 35%, QRSd > 150 ms, and LBBB morphology. The goal is to improve symptoms and reduce morbidity and mortality [18].

If the conditions are the same as in the paragraph above with a difference in QRSd (130 - 149 ms), CRT should still be considered [18].

# 5 Ultra-high frequency ECG analysis

The ultra-high frequency ECG (UHF-ECG) technique was first introduced by Jurak et.al [2]. UHF-ECG is an approach with the ability for more accurate identification of the temporal-spatial distribution of ventricular electrical depolarization and to evaluate the degree of ventricular dyssynchrony. The first step in the UHF-ECG technique is the assesment of ECG signals, which are usually sampled at a frequency of 5,000 Hz (depending on the setting and version, it can even work at 1,000 [3] or 4,000 Hz) with a dynamic range of 26 bits (some version have range 16 or 24 bits) and a frequency range of 2 kHz [2].

Necessary preprocessing steps are the removal of pacing artifacts in patients with pacemakers [19] and the detection of QRS complexes [20], which are then clustered into categories by their morphology [21]. This technique is primarily focused on the dominant QRS morphology (only QRSs from the major morphological group should be further used).

The Fourier and Hilbert transforms were used to compute nine amplitude envelopes in the 150–1050 Hz frequency range [4]. The count of frequency bands has evolved during development of UHF-ECG and it also depends on the sampling frequency of the signal. The amplitudes are averaged with an R–wave trigger and smoothed in the 0–40 Hz passband (UHFQRS) [2].

In Fig. 5.1 averaged QRS complexes from V1-V6 precordial leads could be seen. The envelopes of the UHFQRS complexes from the mentioned leads are shown in Fig. 5.1 b. From this, maps (Fig. 5.1 c) were created, where each row represents the normalized shape of the QRS complex for the corresponding lead. The values were normalized between 0 which is the minimum (blue) and 1 corresponding to the maximum (red).

In order to numerically identify ventricular electrical dyssynchrony, the parameter UHFDYS (Fig. 5.1 e), defined as the difference in the locations of maxima in leads V1 and V6 is computed. According to the UHFDYS parameter in Fig. 5.1, peak depolarization in the right ventricle septum starts 84 milliseconds before peak depolarization in the left ventricle lateral wall. This value can easily be seen from UHFQRS (Fig. 5.1 b–e), but not from conventional (low-frequency) QRS (Fig. 5.1 a, d). In this case, the dyssynchrony between V2-V6 is even bigger than that between V1-V6, so electrical activation map (Fig. 5.1 c) is equally important for us as Fig. 5.1 e [2].

UHG-ECG analysis and UHFQRS is a method which clinical potential lies in detecting the value of ventricular electrical dyssynchrony and thus improving the selection of patients who could respond to CRT. Additionally, the UHF-ECG method has been experimentally used in His bundle pacing [22], RV pacing, and left sep-

tal pacing to optimize the electrode position and analyze the synchrony of heart ventricles.

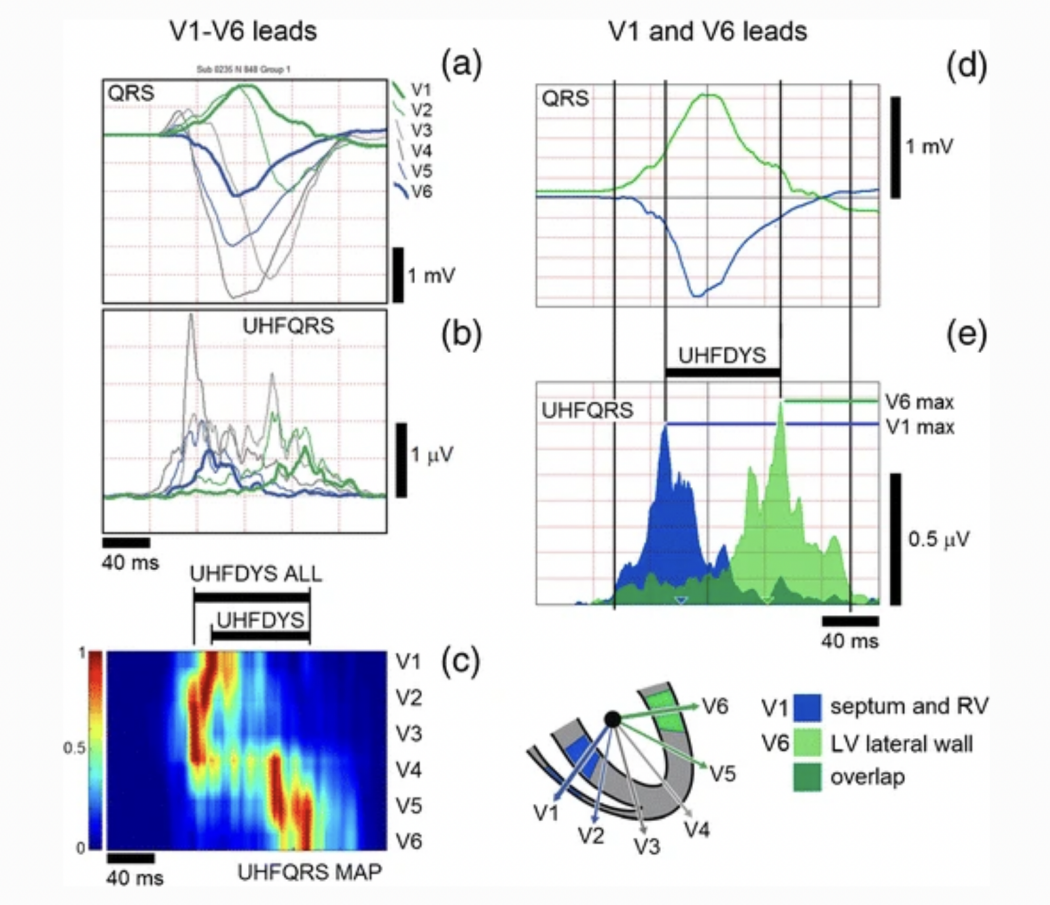


Fig. 5.1: UHF-QRS and UHF-QRS maps. a.) averaged QRS complexes, b.) UHF-QRS envelopes, c.) UHF-QRS maps where each row represents the normalized shape of the QRS complex for V1-V6 leads, d.) averaged QRS, e. ) averaged UHFQRS, UHFDYS—difference in positions of UHFQRS maxima in leads V1 and V6. The maximum intraventricular dyssynchrony is represented by UHFDYS ALL. The V1 lead is represented by the blue color, the V6 lead by the color light green and the overlap of the V1 and V6 depolarization is represented by the color dark green [2].

Even though UHF-ECG analysis results bring many benefits to patients, it still has some drawbacks that can be further improved. This method is very computationally intensive and preprocessing steps such as the removal of pacing artifacts and detection of QRS complexes with subsequent clustering result in excessive computations. Therefore, to improve real-time UHF-ECG analysis performance, it is beneficial to reduce the preprocessing pipeline required for QRS detection and pacing stimuli removal. We believe that using deep learning models will help us achieve that.

# 6 Deep learning

Deep learning (DL) is a specific subset of machine learning (ML) which is one of the branches of artificial intelligence (AI). AI simulates human cognition using computational modelling. ML as a branch of AI helps software applications to gradually improve their accuracy without having to be explicitly programmed to do so. In order to predict new output values, machine learning algorithms use historical data as input. DL is inspired by the structure of the human brain and uses a multi-layered structure of algorithms called neural networks. While a shallow neural network can still make approximate predictions, additional hidden layers can help to optimize and refine for accuracy. Deep neural networks are simply neural networks with 3 or more layers. The initial benefit of deep learning over machine learning is that feature extraction is unnecessary. Feature extraction refers to the process of transforming raw data into numerical features that can be processed while preserving the information in the original data set. Feature extraction is typically a difficult process that requires an in-depth understanding of the problem domain. This step is already included in networks with deep architecture [23].

One of the most popular deep neural network architectures are Convolutional Neural Networks (CNNs) [24]. They are extremely successful at image processing, but also for many other tasks such as speech recognition or natural language processing. The state-of-the-art CNNs have usually 12 layers and more, so they are part of DL. A CNN consists of several computational layers of neurons. The 3 basic types of layers are convolutional layers, pooling layers, and fully connected layers [23].

The main point of convolutional layers is to extract distinctive features from the input which can be an image, video, or time series. The mathematical operation that is applied to the image in the form of a filter is called convolution. The kernel, representing the filter, is a matrix of numbers that simulates weights. A matrix with a certain number of rows and columns is shifted, in other words, convolved over an input, to obtain the resulting feature map. The initial layers of the network distinguish simple visual elements such as edges, corners, or curves. In deeper layers, filters specialized for distinguishing more sophisticated objects could be found [23].

The role of pooling layers is to reduce the spatial resolution of the feature maps while remaining invariant to the shape and position of significant features that have been detected in the image. After the application of the convolution, the predefined neighborhood of pixels is unified into a single value. Typically, MaxPooling layers are used, which extract the maximum from neighboring pixels, but other methods such as MinPooling, AveragePooling, or MedianPooling can also be used [23].

The convolutional and pooling layers are repeated several times, and finally, all

the features are connected using fully connected layers, which are usually present in a traditional multilayer neural network [23].

CNNs are one of the biggest trends in image and signal processing nowadays because they use a special architecture well adapted for classification, detection, and also regression. Medical research in the field of convolutional neural networks is no exception.

ECG is one of the fundamental examination methods in cardiology. In recent years, a number of high-impact studies using deep learning to analyze and classify ECGs in large patient cohorts were published [25, 26, 27]. In the next chapters, deep learning methods will be presented, focusing on UHF-ECG analysis, the results of which can improve patient selection for CRT and even accelerate and refine optimization during pacemaker implantation.

# 7 QRS complex detection in UHF-ECG

The entry point to the UHF-ECG analysis is the detection of the QRS complex. Although this may seem like a simple task, UHF-ECG is specific for several reasons. One is the high sampling frequency for which traditional QRS detection methods have not been refined. But mainly it is the presence of pacing stimuli (Fig. 7.1) in patients with pacemakers, which amplitude is often much higher than the amplitude of a regular ECG signal, and further analysis requires suppression or even complete removal of these artifacts. The current version of the VDI Vision software (desktop application to acquire, process, and analyze UHF-ECG signals in real-time) [4] and its solution for QRS detection requires the removal of pacing stimuli. The F-score of this detector is currently at 90%, which requires improvement because subsequent analysis steps such as QRS morphology clustering are affected by non-captured QRSs that prolong a measurement time. Of course, a longer analysis means longer surgery time for the patient. Thus, our goal is to improve the success rate of QRS detection and thus reduce the measurement time, and speed up pacing optimization which would lead to a shorter surgery time.

The data, methods, and results presented in this chapter were published and presented at the Computing in Cardiology conference in Brno 2021 [28].

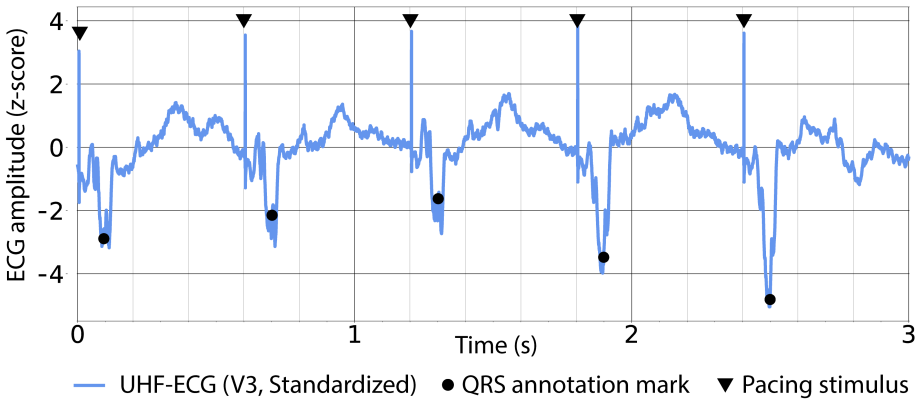


Fig. 7.1: Standardized UHF-ECG signal with bipolar septum stimulation from V3 lead with pacing stimuli (triangles). Circles point to QRS complexes [28].

## 7.1 Data

For QRS complex detection we used a private dataset from Fakultní nemocnice u sv. Anny (FNUSA) hospital (Brno, Czechia) for training and validation. This dataset contained 3,018 12-lead records that were sampled at a frequency of 5,000 Hz. It

consisted of 68 healthy and 942 CRT subjects, and the dataset included signals with spontaneous and paced QRSs. A total of 2,250 ECG recordings acquired from 780 subjects were used as a training set; other 768 ECG records (450 spontaneous and 318 paced) acquired from 240 subjects were used as a validation set. The QRS complex annotation marks for training and validation were automatically created by the VDI Vision software [4].

An independent private dataset from Fakultní nemocnice Královské Vinohrady (FNKV) hospital (Prague, Czechia) was used to test the model. The data were also sampled at a frequency of 5,000 Hz and included 12-lead records. The test set contained 300 recordings obtained from 47 subjects before, during, and after pacemaker implantation. These records contained spontaneous QRSs (57 records from 11 subjects) and paced QRSs (247 records from 47 subjects). Subjects in the test set were mostly treated by His bundle or Parahisian stimulation. Several recordings were obtained for different pacing electrode positions per patient. QRS complex annotation marks were manually prepared using the SignalPlant software [29].

QRS complex annotation marks were converted to QRS complex probabilities. In the region of the QRS complex, more specifically 0.05 s (250 samples) to each side of the QRS complex annotation mark, the probability was set to 1; everywhere else, the probability was set to 0 and a rectangular signal of the same length as the input signal was produced.

## 7.2 Method

CNN with UNet architecture was chosen for QRS complex detection. Since the model needs to work in a real-time application, a 3 seconds input window was chosen. Neural network process 3 precordial leads (V1, V3, V6). Thus the input of the UNet architecture is a matrix of size 3x15,000 (3 s x 5,000 Hz). After UNet inference, we get an output of length identical to the length of the signal. This output is pushed through a softmax activation function, which allows us to obtain the probability of QRS/nonQRS complex for each sample (Fig. 7.2).

## 7.3 Preprocessing and data augmentation

The described method is developed to work in real time with minimal signal preprocessing. Before network inference, it is necessary to standardize the signal using a z-score only.

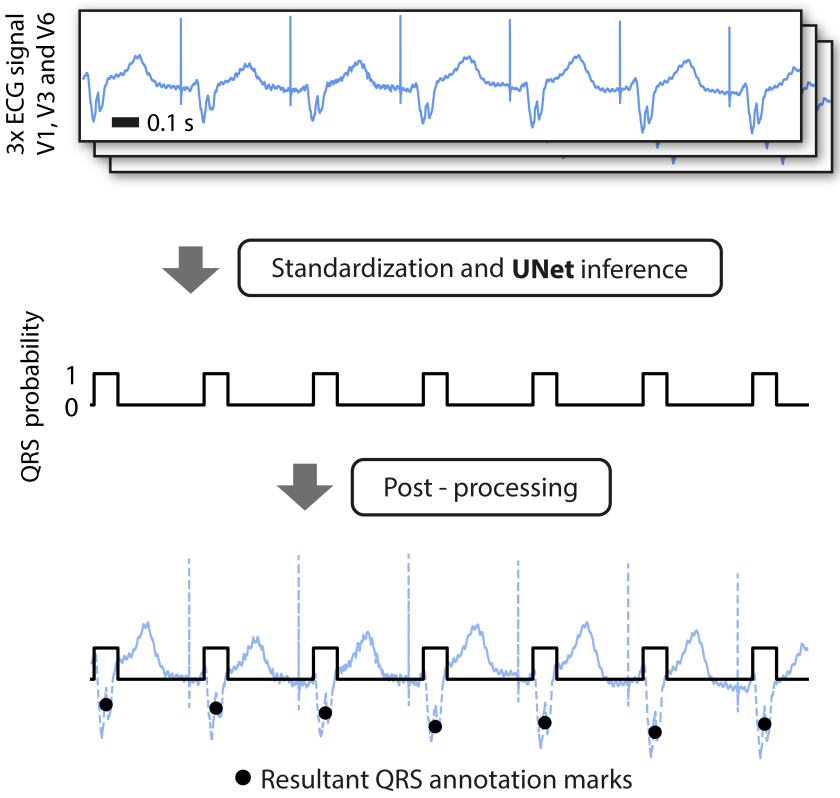


Fig. 7.2: QRS detection method. Top - original ECG signal (V3 lead). The signal (ECG leads V1, V3, and V6) is standardized and pushed into the UNet model, resulting in a QRS probability vector (middle). Post-processed output probability results in QRS annotation marks (bottom) [28].

To extend the training dataset and simulate signals with faster heart rates, we chose online augmentation of random recordings in the training dataset. From these recordings, a 3-second signal window was prepared. A random distant segment of length 6 seconds was selected and resampled to a sampling rate of 2,500 Hz using a Butterworth antialiasing filter (the fifth-order with a cut-off frequency of 1,200 Hz, and decimation with factor 2) [30].

## 7.4 The neural network architecture

For the deep learning model, the UNet architecture was chosen, which was originally developed for image segmentation [31]. Since in our case we are dealing with 1D signals, all the layers are changed into one dimensional form. The main difference between our architecture and the original one is the different hyperparameters in the max pooling and convolutional layers and the size of the kernels in the convolutional

layers.

The UNet architecture consists of two symmetric parts, the contraction (Fig. 7.3 -left) and expansion (Fig. 7.3 -right) sections. In the contraction section, there is a reduction in signal length and an increase in the number of feature maps. There are 4 identical blocks which consist of 2 convolution layers (kernel size = 9, stride = 1, padding = 4), batch normalization, and ReLU activation function followed by MaxPooling layer (kernel size = 2, stride = 2). After each block signal is downsampled with a factor of two and the number of feature maps in the first three blocks doubles.

Similarly to a contraction section, there are 4 blocks in the expansion section. In each block, there is a transpose convolution layer (kernel size = 9, stride = 2) which upsamples the signal length by a factor of two. The transpose convolution layer is followed by two convolution layers (kernel size = 9, stride = 1, padding = 4) with batch normalization and ReLU activation function. Output from each block is concatenated with output from a corresponding block in the contraction section, and after the first three expansion blocks feature maps number is cut in half.

The final layer of the network is the convolution layer (kernel size = 1, stride = 1) with a softmax activation function that outputs the class probabilities [32].

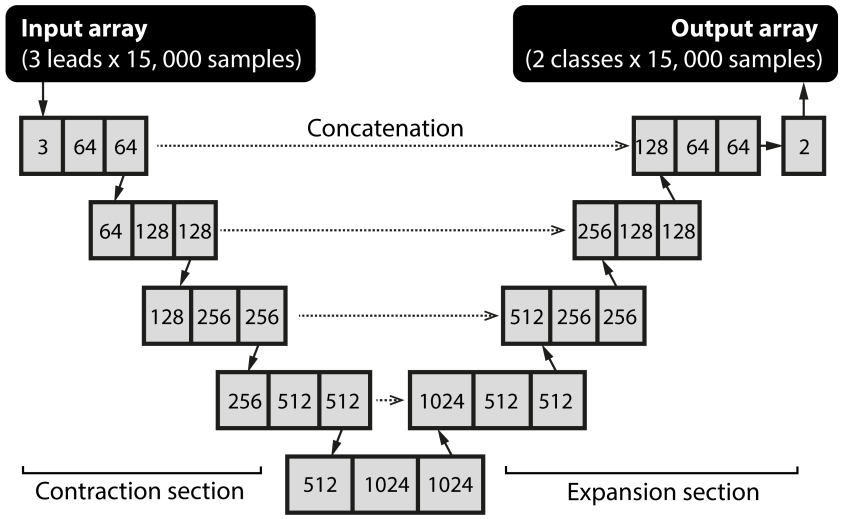


Fig. 7.3: UNet architecture [28].

## 7.5 Postprocessing and training

In order to obtain accurate QRS complex positions, it is necessary to post-process the output from the network, which is in the form of the QRS complex probability.

For this, a probability and distance criterion was chosen empirically on the validation dataset. Only that part of the signal is chosen as QRS complex which has a probability above 0.95 and is at least 10 ms long (40 samples). The final QRS position is chosen as the midpoint of this segment.

The model had been trained for 30 epochs, using Adam optimization [33] with a learning rate of 0.0001. Weighted cross-entropy loss function was used due to imbalanced output classes (QRS/nonQRS) [34]. We used a graphic-processing unit (GPU) with "Compute Unified Device Architecture" (CUDA) for training (GeForce RTX 2080 Ti). The methods were implemented in the Python programming language version 3.8.6 [35]. The PyTorch library was used for the creation of the convolutional neural network and its optimization [36].

## 7.6 Results

The success rate of the method is reported in Tab. 7.1. Results are presented for the entire FNKV test dataset but also separately for spontaneous and paced QRSs. The results were evaluated in terms of sensitivity, which indicates the proportion of missed QRSs, positive predictive value (PPV), which indicates the proportion of falsely detected QRSs, and F-score, which is the harmonic mean of sensitivity and PPV.

Furthermore, the proposed model performance was compared to the method already used in VDI vision (up to version 1.0) and to the Pan-Tompkins algorithm for QRS detection (Tab. 7.2) [37].

Tab. 7.1: QRS detection model results for used datasets. No. of QRS refers to the total number of QRSs in records. Sens represents sensitivity, PPV is a positive predictive value.

| **Dataset** | **No. of QRS** | **Sens [%]** | **PPV [%]** | **F1-score [%]** |
|---|---|---|---|---|
| **Train** | 7,904 | 98.99 | 97.42 | 98.19 |
| **Validation** | 2,745 | 98.36 | 96.95 | 97.65 |
| **Test (total)** | 1,480 | 96.49 | 97.74 | 97.11 |
| **Test (spontaneous)** | 214 | 97.20 | 95.41 | 96.30 |
| **Test (stimulated)** | 1,266 | 96.37 | 98.15 | 97.25 |

Tab. 7.2: Comparison of performance for specific QRS detection models on the test set (300 records from 47 patients). Results are reported for spontaneous and paced records and for the entire test set (Total). VDI refers to the detection method used in software VDI vision version 0.9 or earlier.

| Model | Record type | Sensitivity [%] | PPV [%] | F1-score [%] |
|---|---|---|---|---|
| | Spontaneous | 97.20 | 95.41 | 96.30 |
| **Unet** | Paced | 96.37 | 98.15 | 97.25 |
| | Total | 96.49 | 97.74 | 97.12 |
| | Spontaneous | 92.52 | 94.29 | 93.40 |
| **VDI** | Paced | 86.97 | 93.07 | 89.91 |
| | Total | 87.77 | 93.25 | 90.43 |
| | Spontaneous | 81.31 | 75.98 | 78.56 |
| **Pan Tompkins** | Paced | 29.51 | 28.55 | 29.02 |
| | Total | 37.1 | 35.7 | 36.39 |

## 7.7 Discussion

In this chapter, we introduced a deep-learning model aimed at QRS complex detection in UHF-ECG recordings. The achieved F-score for the test dataset (97.11 %) is better than the F-score (90.43%) of the QRS detector embedded in the current version of the VDI vision software.

Additionally, we compared the Pan Tompkins detector implemented in the Python package "py-ecg-detectors" version 1.0.2 with our model. On the test set, the Pan Tompkins received an F1-score of 29.02% for stimulated recordings and 78.56% for spontaneous activity compared to our 96.30% and 97.25% for stimulated and spontaneous activity, respectively. The Pan Tompkins detector, however, was not intended for UHF-ECG recordings with paced QRSs, which relates to a nearly 50% difference in F1-score between paced and spontaneous signals (Tab 7.2).

We also explored the most typical cause of false positives (FP) and false negatives (FN). The most frequent occurrence of FP detections is at the beginning and at the end of the 3-second window, so it is recommended not to include the first and last 0.5 seconds of the ECG record in the analysis. Ventricular fusion beats with random stimuli in their descending edge have the highest non-captured QRS rates (FN). However, as only the majority morphological group of QRS is examined in further UHF-ECG analysis, these FN detections have no negative effects. If caught, fusion beats would be removed from the examination.

# 8 Extension for QRS onset and offset detection

In the next step, we decided to extend the detection model to deliver the onset and offset positions of the QRS complex and thus estimate the QRS duration (QRSd). The prolonged duration of QRS complex in a 12-lead ECG is associated with adverse prognosis in patients with cardiac disease. It is one of the parameters and typical measurements linked to conduction abnormalities in the heart ventricles. QRSd describes the time difference between the start (QRS onset) and end (QRS offset) of ventricular depolarization. A healthy, young population usually has low QRSd, around 70-80 ms, while patients with conduction diseases have QRSd higher than 110 ms [38]. Since the QRSd can be easily read from printed ECG, it is an essential metric for cardiologists. The data, methods, and results (with some alterations) presented in this chapter were published and presented at the Computing in Cardiology conference in Tampere 2022 [39].

## 8.1 Data

In this case, we have 2 tasks, that must be completed by one method in one inference step: the first is detecting the QRS complex and the second is delivering the QRSd. For training, validation, and testing of QRS detection, data from the same institutions as in the section 7.1 were used. This time we were able to add new data to the training, validation, and test.

In terms of QRS duration assessment, all the datasets mentioned above were used, plus external public datasets for testing which had information about QRSd. Unfortunately, these datasets could not be used to assess QRS detection because they only contained median QRS information.

For cross-database tests, we selected four independent datasets: a private dataset from FNKV hospital (extended with new recordings) and 3 public datasets; Cipa [40], LUDB [41] and Strict LBBB [42]. These public datasets contain only records with spontaneous rhythm. The duration of the QRS complexes for FNKV (testing) and FNUSA (training, validation) datasets was obtained from an automatic detector based on wavelet transform [43]. This detector was the most accurate in the challenge LBBB Initiative of the ISCE 2018 meeting [42], where a reduced subset of MADIT-CRT data [44] was used. The boundaries of the QRS complexes for the public datasets were determined by certified cardiologists by manual inspection of each ECG recording.

The desired output of the network for FNUSA and FNKV data was constructed from QRS annotation marks and QRS duration annotations. Each QRS annotation mark of an ECG record belongs to one of three most common morphological groups, and each of these morphological groups has a corresponding onset and offset, thus corresponding duration. Based on this, for each recording, we built a rectangular signal representing ongoing ventricular depolarization: samples between QRS onset and offset of particular QRS were set to 1, and all the other samples remained at zero. In contrast to the QRS detection model, these rectangles are no longer of a fixed duration of 10 ms; their size corresponds to the QRS duration of the associated ECG recording and corresponding QRS morphological group. An overview of the data used for validation and testing is summarized in Tab. 8.1.

Tab. 8.1: Datasets used for validation (FNUSA) and cross-database tests (FNKV, Cipa, Strict LBBB, LUDB) for the QRS duration model. The Rhythm column tells whether the recordings were spontaneous (spont) or paced, and the Recordings column tells the number of recordings for a given dataset.

| Database | Sampling frequency [Hz] | Rhythm | Recordings |
|---|---|---|---|
| **FNUSA** | 5,000 | Spont | 206 |
| | | Paced | 239 |
| **FNKV** | 5,000 | Spont | 371 |
| | | Paced | 1,941 |
| **CIPA** | 1,000 | Spont | 5,749 |
| **Strict LBBB** | 1,000 | Spont | 602 |
| **LUDB** | 500 | Spont | 200 |

## 8.2 Method

The same method was used to detect QRS onset and offset as for QRS detection, with small variations that allowed us to achieve better accuracy.

Firstly, in preprocessing, in addition to the z-score, resampling to 5,000 Hz was included for all datasets, as this model was designed to work primarily on UHF-ECG data.

Secondly, 12-lead ECG was used instead of 3-lead ECG, so the number of the model input channels was 12.

Next, each BatchNormalitaztion layer was changed to an InstanceNormalization layer. BatchNormalization layers behave differently in training and in evaluation

mode, replacing them with InstanceNormalization allowed us to achieve better results in this case.

The hyperparameters of the architecture were also changed, the sizes of the kernels and strides were in this case 12 and 6 or 5, respectively.

Furthermore, the loss function was changed. The Mean square error loss function was added to the weighted crossentropy function, which allowed better penalization of the samples in the QRS onset and offset region.

The output of the network is an array of QRS probabilities (Fig. 8.1). To obtain the final QRS positions and thus their durations, the output must be post-processed. Segments of the output signal are considered QRS if their probability is higher than 0.7 and their duration is at least 50 ms (empirically determined on a validation FNUSA dataset). If two consecutive QRS complexes have a distance of less than 60 ms, they are combined into a single QRS complex segment. The initial and final 100 ms of the utilized 3s signal segment are not included in the final QRS duration and detection result calculations.

## 8.3 Results

The performance of the model in terms of QRS detection for datasets that contained information about the QRS position in the signal is shown in Tab. 8.2. Results are reported separately for paced and spontaneous records.

Tab. 8.2: Results for QRS detection task for validation (FNUSA) and test (FNKV, LUDB) datasets. PPV refers to the positive predictive value. Spont stands for spontaneous.

| **Database** | **Rhythm** | **Sensitivity** [%] | **PPV** [%] | **F-score** [%] |
|---|---|---|---|---|
| **FNUSA** | Spont | 99.83 | 99.15 | 99.49 |
| | Paced | 99.43 | 99.43 | 99.43 |
| **FNKV** | Spont | 99.29 | 98.86 | 99.07 |
| | Paced | 99.36 | 99.28 | 99.32 |
| **LUDB** | Spont | 96.96 | 99.35 | 98.14 |

To validate the ability of the model to estimate QRS duration, Mean absolute error (MAE), Standard Deviation of MAE (STD), and Median Absolute Error (MedAE) were calculated between the duration annotations and the duration obtained after postprocessing the network output (Tab. 8.2).

Tab. 8.3: Results for QRS duration task for validation (FNUSA) and test (FNKV, LUDB, CIPA, LBBB) datasets. MAE refers to the mean absolute error, STD refers to the standard deviation of the absolute error and MedAE is the median average error. Spont stands for spontaneous.

| **Databae** | **Rhythm** | **MAE [ms]** | **STD [ms]** | **MedAE [ms]** |
|---|---|---|---|---|
| **CIPA** | Spont | 13.30 | 5.90 | 13.10 |
| **LUDB** | Spont | 10.02 | 9.69 | 7.34 |
| **LBBB** | Spont | 15.46 | 8.03 | 15.40 |
| **FNUSA** | Spont | 7.56 | 7.62 | 4.88 |
| | Paced | 6.58 | 8.88 | 3.67 |
| **FNKV** | Spont | 9.69 | 10.12 | 6.4 |
| | Paced | 12.80 | 15.81 | 7.44 |

As mentioned above, FNUSA and FNKV datasets contained information of QRS duration for the 3 different morphological groups. Tab. 8.4 shows the results separately for these morphological groups. In this case, the duration of each network-detected QRS complex was separately compared with the corresponding annotated QRS complex. In each recording, the mean QRS duration for each morphological group was calculated.

Tab. 8.4: Results for QRS duration task for validation (FNUSA) and test (FNKV) datasets for 3 different morphological groups. MAE reffers to the mean absolute error, STD refers to standard deviation of the absolute error.

| **Database** | **Morphological group** | **No of QRSs** | **MAE [ms]** | **STD [ms]** |
|---|---|---|---|---|
| | 1 | 1,216 | 6.68 | 7.95 |
| **FNUSA** | 2 | 64 | 14.37 | 17.52 |
| | 3 | 20 | 14.71 | 24.75 |
| | 1 | 8,328 | 11.88 | 15.12 |
| **FNKV** | 2 | 764 | 15.71 | 20.14 |
| | 3 | 405 | 14.71 | 17.21 |

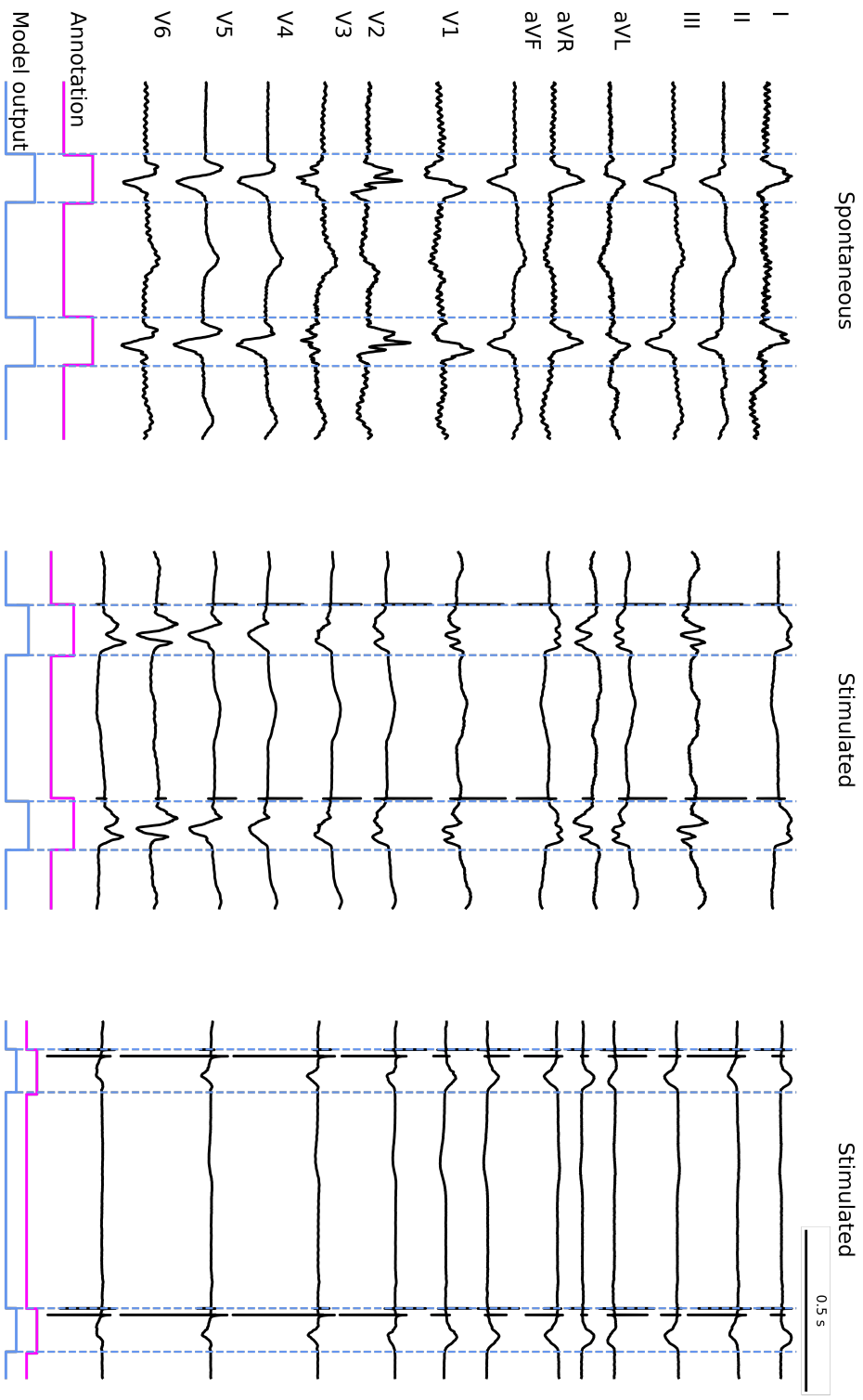


Fig. 8.1: Example of QRS onset and offset estimation for 3 different 12-lead UHF-ECG signals (1 spontaneous and 2 stimulated/paced). The purple rectangular signal represents the annotations and the blue rectangular signal represents post-processed model output [28].

## 8.4 Discussion

In this chapter, we introduced a deep learning model that delivers the onset and offset of the QRS complex in addition to the QRS complex position and hence its duration in one inference step. The models differ from the QRS detection model in the number of data used for training, hyperparameters of the network architecture (size of kernels, 9 vs. 12), and loss function used for training (weighted crossentropy vs. weighted crossentropy + MSE) but more importantly, they differ in the size of the annotation "rectangle," which forms a signal that a model is trained to produce. These rectangles are no longer of a fixed duration of 10 ms; their size corresponds to the QRS duration of the associated ECG recording and an associated morphological group of the QRS complex.

We received an overall F-score of 98.84 $\pm$0.51% for test datasets (FNKV, LUDB) for QRS detection task (Tab. 8.2). In terms of the QRS duration task, we received an overall MAE of 12.25 $\pm$2.16 ms (Tab. 8.3) for test datasets (CIPA, LUDB, LBBB, FNKV). We also compared results between the 3 morphological groups (Tab. 8.4). We observed slightly worse results for morphological groups 2 and 3 compared to morphological group number 1. This difference reflects the distribution of morphological groups in the training set.

# 9 Pacing stimuli removal

The current method for UHF-ECG analysis requires the removal of the pacing stimuli. This is an essential step for QRS morphology clustering. While deleting a stimulus' rising edge is rather simple, it is more difficult to localize and remove the end of the post-stimulus recharge phase because of its low amplitude. The current method for removing pacing pulses and the area around them requires detecting them and then applying a linear function supplemented by a spline function on the edges in the time domain [19]. In this technique, however, the useful part of the signal at the stimulus location is removed. Our task is to develop a regression deep learning model that is able to suppress the effect of the pacemaker while maintaining a useful signal.

## 9.1 Data and preprocessing

We used data from the FNUSA hospital to train and validate the model for pacing stimuli removal. For testing, we used independent data from the FNKV hospital. The number of records used can be found in Table 9.1.

Tab. 9.1: Number of patients used for removal of pacing stimuli for training, validation and test set.

| | **Train** | **Validation** | **Test** |
|---|---|---|---|
| **Database** | FNUSA | FNKV | FNKV |
| **Spontaneous** | 639 | 310 | 112 |
| **Paced** | 384 | 74 | 112 |

Signals containing V1- V6 precordial leads were extracted from the database. We also extracted corresponding target signals for the model with pacing stimuli suppressed and replaced by a linear function supplemented by a spline function on the edges as a target (PCM1-PCM6) [19].

Our dataset contains paced and spontaneous data. Paced leads (V1-V6) have corresponding leads without pacing pulses as a target (PCM1-PCM6). Regarding spontaneous data, online augmentation was performed. Randomly, a portion of the signals remained spontaneous with the same target as the input to the model. For the portion of the spontaneous signals, stimulus pulses were artificially created in the area of QRS complex. For each of these signals, the number of pacing stimuli within the input window (1-3), their polarity, amplitude (0.5 - 3 x the amplitude of the spontaneous signal), and position within the input window were randomly

selected. The corresponding target was spontaneous signal without these artificial changes.

A 0.2 s (1000 samples) input window is taken from each signal. Each precordial lead from a signal enters the model separately. In this window, 1st derivative and then z-score normalization is applied. The process of generating data for training and preprocessing is summarized in Figure 9.1.

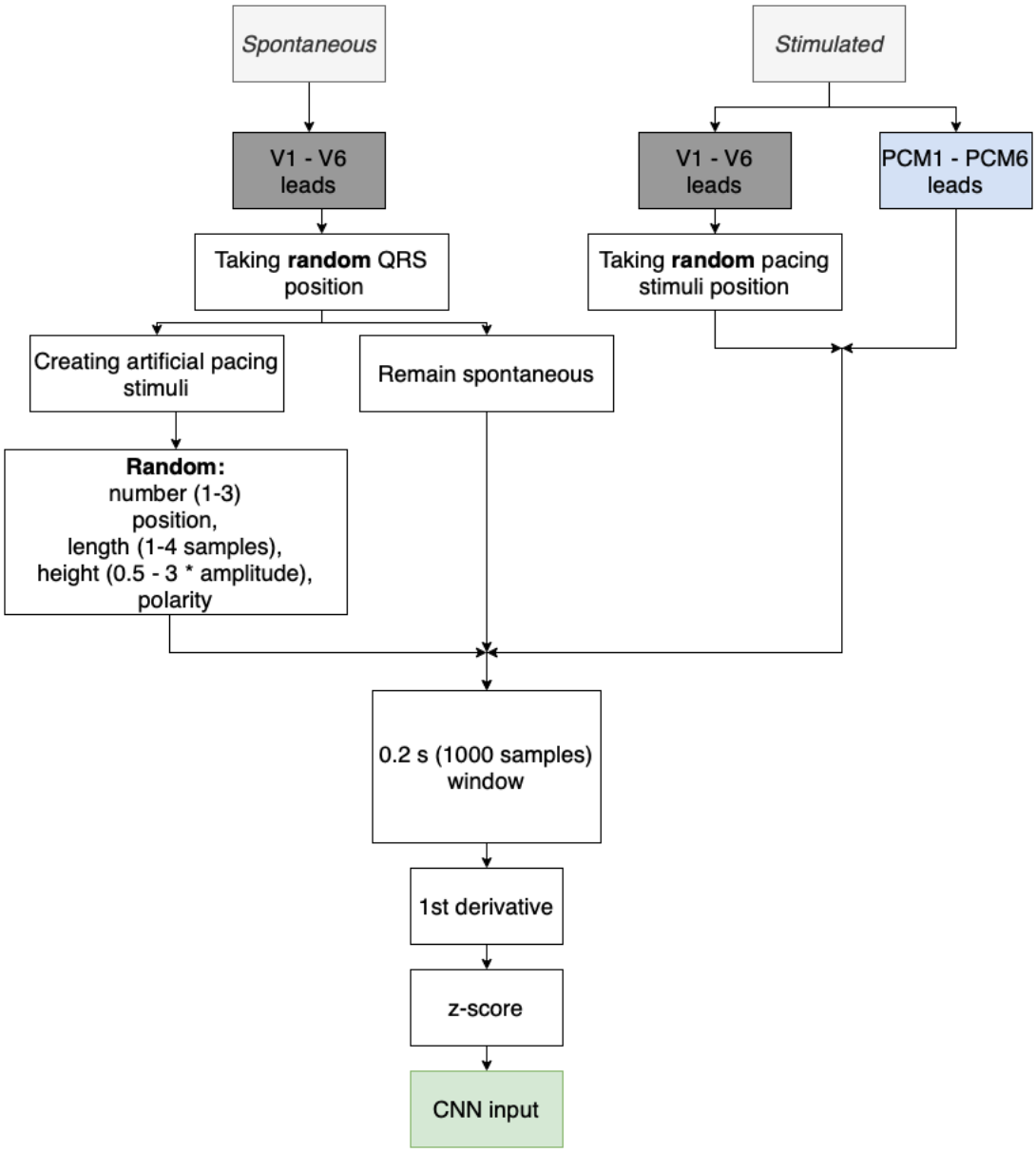


Fig. 9.1: Scheme of preprocessing and generating data for training.

## 9.2 Model

The deep learning model used for removing pacing stimuli from UHF-ECG was pix2pix [48]. This model was originally developed to map any image to any other image, e.g. the edges of an object to the image of the object. In our case, we are mapping the signal to the signal of the same length minus the pacing stimuli, so we need to transform all the layers into 1D. Model architecture belongs to a group of models called conditional Generative Adversarial Networks (cGANs). It consists of a generator and a discriminator.

The generator is a CNN with UNet architecture. An input to the network of size 16x1x1,000 (batch size x 1 precordial lead x signal length) passes through the generator and the output is a signal of the same length.

The discriminator is a classification CNN consisting of 4 identical blocks containing a convolutional layer( kernel size = 4, stride = 2), an instance normalization layer and leaky ReLU activation function (negative slope = 0.2). The input to this network is 16x2x1,000 (batch size x concatenated leads x length of the signal) After each of these layers, the number of feature maps is increased (64, 128, 256, 512). Finally, one convolutional layer is applied (kernel size = 4, stride =2) whose output has a size of 16x1x61. The input of the discriminator network is either the output of the generator concatenated with the input of the generator or the target of the generator with the input of the generator.

### 9.2.1 Training the generator

To train the generator, its inference is done first. The input to the generator is a stimulated signal (16x1x1,000). Then its output is concatenated with its input and such a tensor of size 16x2x1,000 enters the discriminator. To train the generator we use 2 error functions which are finally summed. L1 loss measures the L1 distance between the generator's target and its output. Furthermore, the loss from the discriminator, the MSE between the output of the discriminator (16x1x61) and a vector of ones of the same length (16x1x61) is computed. The final loss from the generator is therefore (10 x L1 loss) + MSE loss (Figure 9.2). When this loss is back-propagated, the discriminator network's parameters are frozen.

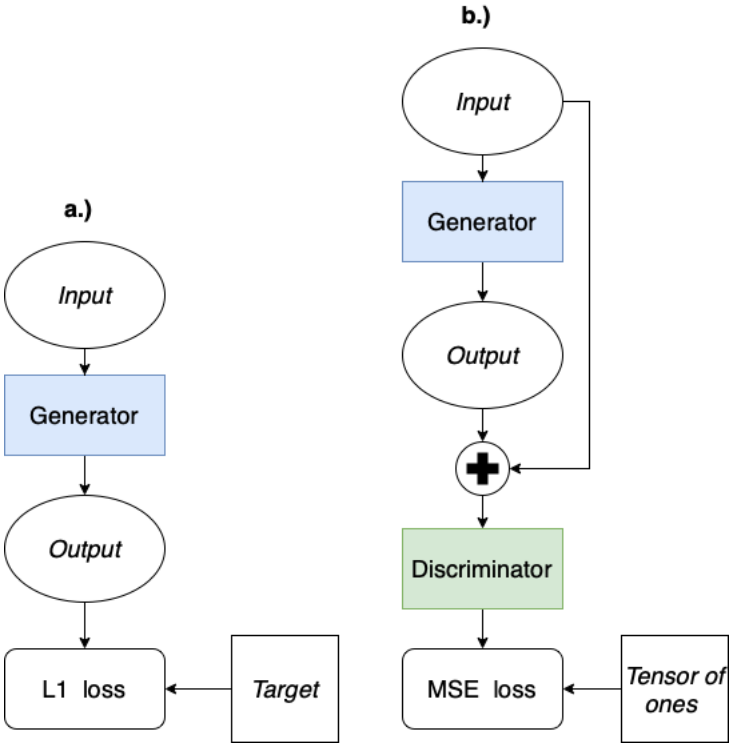


Fig. 9.2: Scheme for training the generator. MSE stands for Mean Square Error. Part a.) of the Figure represents the generator inference and the L1 loss calculation. Part b.) represents the concatenation of the input to the discriminator and calculation of the MSE loss.

### 9.2.2 Training the discriminator

The role of the discriminator is to try to distinguish whether its input is a concatenated generator input with a generator output or with a target. The discriminator loss function measures how good or bad the discriminator's predictions are. When training the discriminator, the generator's parameters are frozen.

Inference of the discriminator is performed 2 times. First, the concatenated input of the generator and target enters the discriminator. The loss function is calculated as MSE of the output of the discriminator and tensor of ones of the exact size as the output (Figure 9.3 a.)).

The second time the input of the generator concatenated with the output of the generator enters the discriminator. The loss function is now calculated as MSE of the output of the discriminator and tensor of zeros of the exact size as the output (Figure 9.3 b.)). The resulting discriminator loss is the sum of the 2 losses mentioned above.

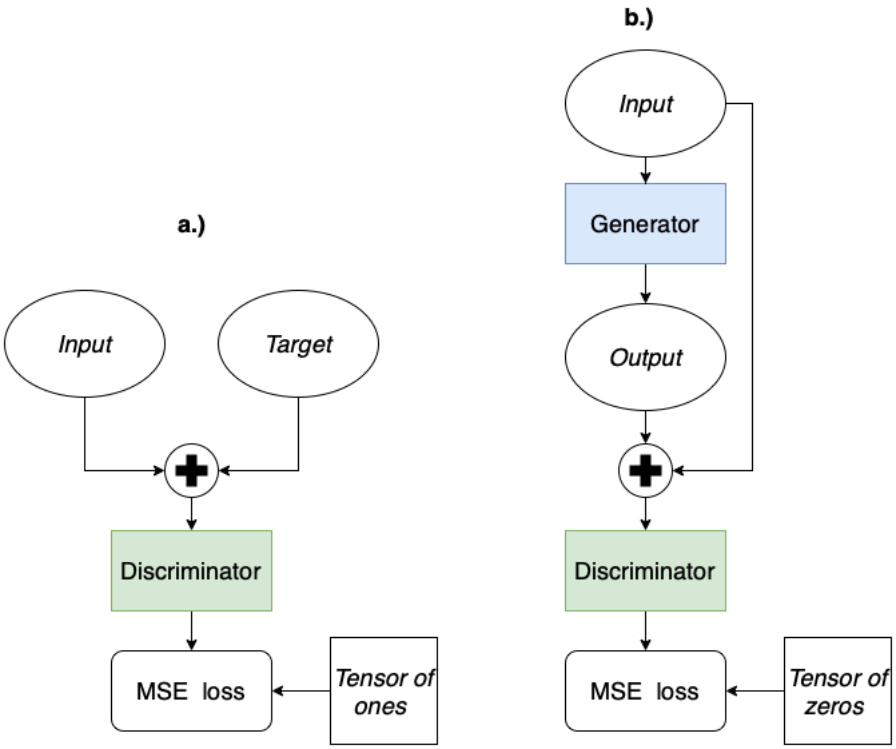


Fig. 9.3: Scheme for training the discriminator. MSE stands for Mean Square Error. Plus stands for concatenation. Part a.) of the Figure represents the first discriminator inference with target and input to the generator concatenated. Part b.) represents the second discriminator inference with output of the generator concatenated with the input to the generator.

## 9.3 Method and results

For further evaluation, the output must be integrated and compared with the original target (before 1st derivative). After training the model, we use only the generator network for inference. The output of the model and its target are the first derivative signals. An example of the input, output and target can be seen in Fig. 9.4.

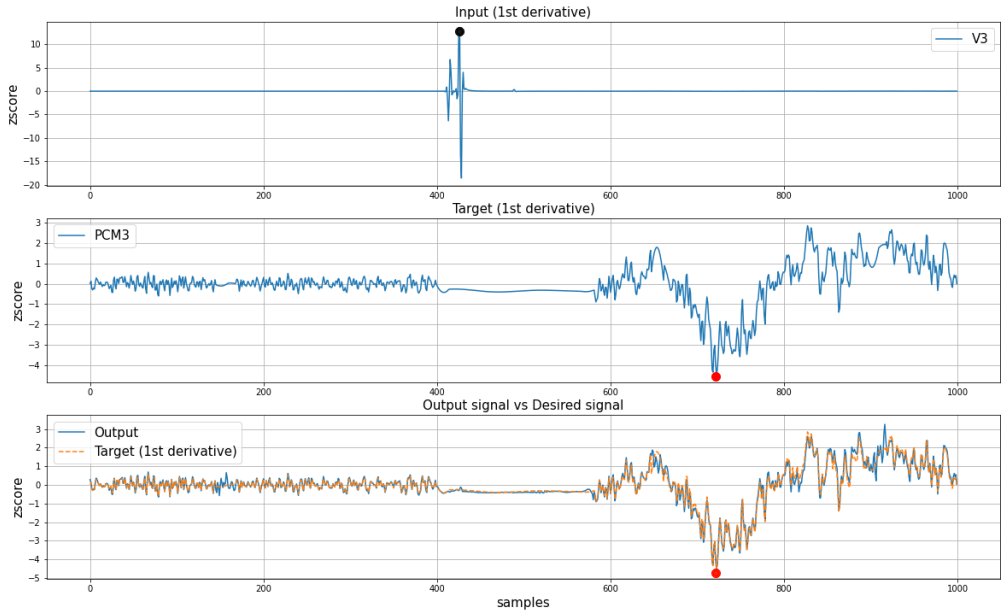


Fig. 9.4: Example of pacing stimuli removal. First subplot represents the input to the network. Second subplot represents the target ECG (processed by the current method implemented in VDI vision software) and third subplot represents the output of the model (blue line) compared to the target (orange line). The black dot is the mark of the pacing stimuli and the red one of the QRS complex.

Then we analyzed the method results on 224 signals from the test set (112 spontaneous and 112 paced). UHF-ECG analysis is performed from amplitude envelopes and therefore it is necessary to find out how the method for pacing artifacts removal affects them. We performed network inference on the whole signals with a floating window of 1,000 samples. We then took 50 ms before and after QRS complex mark, applied Fourier and Hilbert transform and counted 15 amplitude envelopes (150-950 Hz). From these envelopes in the QRS complex region, we created an average envelope for each frequency band and compared this with the average envelope of the target and calculated the Spearman correlation. The results of the correlation of spontaneous and paced data plus 95% confidence intervals can be seen in Figure 9.5.

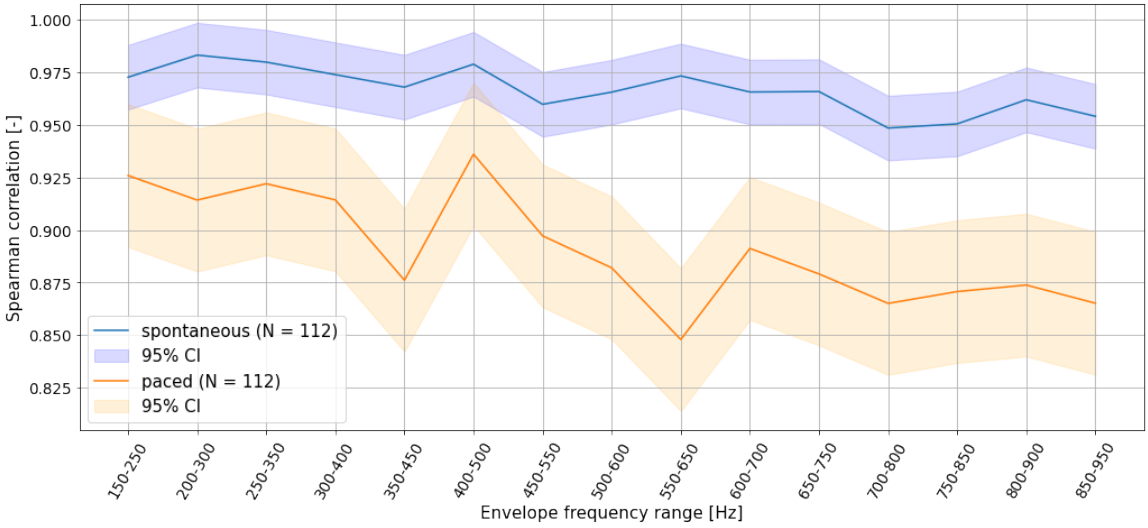


Fig. 9.5: Correlation of average amplitude envelopes in 15 frequency bands between target and model output. CI stands for confidence interval

## 9.4 Discussion

Our goal was to create a deep learning model that would remove the pacing stimuli, but at the same time would not remove the useful signal in the pacing phase and recharge phase. We sought to achieve this by training on paced data but also by creating artificial pacing stimuli in spontaneous ECGs. We evaluated the results based on the correlation of the average amplitude envelopes in 15 frequency bands between the target and the model output in QRS complex region. As expected, when a spontaneous signal enters the model, where there is no need to remove pulses, the network achieves a higher correlation and has smaller confidence intervals. However, for both spontaneous and paced data, there is a tendency that the correlation decreases as the frequency band increases. Hence, although in the time domain, it looks like our model can remove pacing stimuli with minimal mean square error between the output and target signals, if we create frequency band amplitude envelopes we can see that correlation between the target and model output is not sufficient for paced signals.

The advantage over the current method is the stimuli removal in one inference step with no need for previous QRS complex detection. However, regarding amplitude envelopes in different frequency bands and paced ECGs, performance need to be further improved. The results suggest that to apply this method in a real time UHF-ECG analysis, it is necessary to bring the performance of the model on the paced data to at least the same performance level as on spontaneous data.

# 10 Assessing the level of ventricular electrical delay

The ejection fraction, QRS duration (QRSd) and QRS morphology are the main selection criteria for CRT. Because 1/3 of patients, with ejection fraction reduced to lower or equal to 35 % and QRS duration above 150 ms with LBBB morphology do not respond to CRT, a technique for assessing the level of electrical ventricular delay (VED) has been developed in the past [2] [45]. The value of this delay reflects the electrical dyssynchrony between the right ventricle septum and left ventricle lateral wall. Patients with low values for the VED parameter and QRS duration that satisfies the CRT criterion, are not likely to respond to CRT [46]. Measuring the VED parameter may raise the number of patients who react to CRT [3]. The value of this delay is positive for the LBBB morphology and negative for the RBBB morphology. Our task is to develop a deep learning model that would estimate the VED value in a single inference step directly from ECG signal.

## 10.1 Data and preprocessing

For training the regression deep learning model we used data from FNUSA and FNKV hospital. This time, however, the datasets were mixed together due to the fact that the individual datasets contained patients with different types of pathologies. In the FNUSA dataset, there are mainly patients with LBBB morphology, on the other hand in the FNKV dataset there are mostly patients with AV blocks. The VED parameter as ground truth for the model training was calculated as shown in Chapter 5 (referred to as UHFDYS).

We deleted outliers from the dataset based on VED values using an interquartile range. The first and third quartiles are calculated, which are then subtracted from each other to obtain the interquartile range. This is multiplied by 1.5 and the resulting value is subtracted from the first quartile and added to the third quartile forming upper and lower bound. All observations that have VED values outside these bounds are classified as outliers. The distribution of the data in the form of boxplots and histograms is shown in Figure 10.1. The median VED in FNUSA and FNKV are 15 and 6 ms; the randomly selected value of the FNUSA dataset is considered to be greater than the randomly selected value of the FNKV dataset (Mann–Whitney U = 5,643,926, $p < 0.001$ right-tailed), which is precisely due to other types of pathologies between datasets.

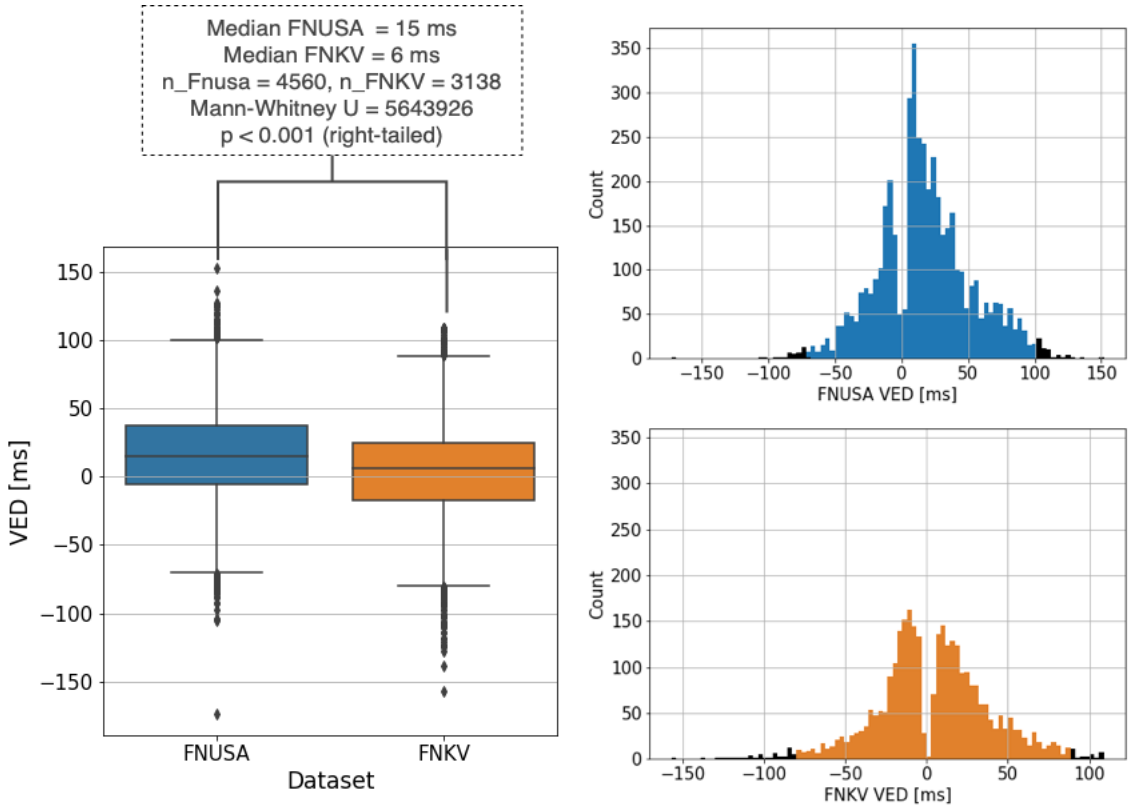


Fig. 10.1: Distribution of VED parameter for data from FNUSA (blue) and FNKV (orange) datasets. Black dots in boxplots and black bars in the histogram represent outliers. Mann–Whitney right-tailed test shows that the randomly selected value of the FNUSA dataset is considered to be greater than the randomly selected VED value of the FNKV dataset ($U = 5{,}643{,}926$, $p < 0.001$).

Data were partitioned into training, validation, and test so that the same patients did not appear between the partitions and also so that the distribution of the VED value was approximately the same in all 3 partitions. For some records, there was no patient information. Thus, all these records were included in the training set to avoid overfitting. The number of patients and records in each split is captured in Table 10.1.

Tab. 10.1: Number of patients and records used for training, validation, and testing the regression model for estimation of VED.

| | **Training** | **Validation** | **Test** |
|---|---|---|---|
| **Number of patients** | 1,384 | 169 | 178 |
| **Number of records** | 6,326 | 592 | 592 |

Our goal is to estimate the value of the VED parameter for the main morphology of the QRS complexes, so we take the 8s of the UHF-ECG signal as input. This is then downsampled to a sampling rate of 1,000 Hz, differentiated and passed through the neural network.

## 10.2 Method

We experimented with several models, different combinations and types of layers. The 2 models that gave the best results on the validation dataset are presented next.

We used 2D and 1D variants of the convolutional neural network for VED assessment. For the 1D variant, the input tensor size is 16x6x8,000 (batch size x number of leads x signal length). The kernel size in the convolutional layers was chosen to be 5 and 7, with zero padding = 2. The number of feature maps was increased to 20 after the first double convolution block and then doubled after each subsequent double convolution block (40, 80, 160, 320). After each of these blocks, a max-pooling layer and a drop-out layer were included. Finally, max-pooling, linear layer, ReLU activation function, and the last linear layer were applied to the tensor of size 16x320x496 to deliver the output of the network.

The 2D variant was based on the 1D variant in terms of architecture, but in this case, the layers are in 2D format. The idea behind this is that the VED parameter is originally estimated from 6 precordial leads simultaneously in time and the time shift between the QRS complex in lead V1 to V6 is tracked, hence we apply 2D convolution so that the network can see multiple leads simultaneously in time. The input to the network is 16x1x6x8,000 (batch size x number of channels x number of leads x length of the signal). The kernel sizes, in this case, were 3x3 with zero padding = 2. Finally, only one max-pooing layer and one linear layer were included. The output consisted specifically of the VED parameter without the need for further postprocessing in both of the architectures. Neural network architectures are depicted in Fig. 10.2.

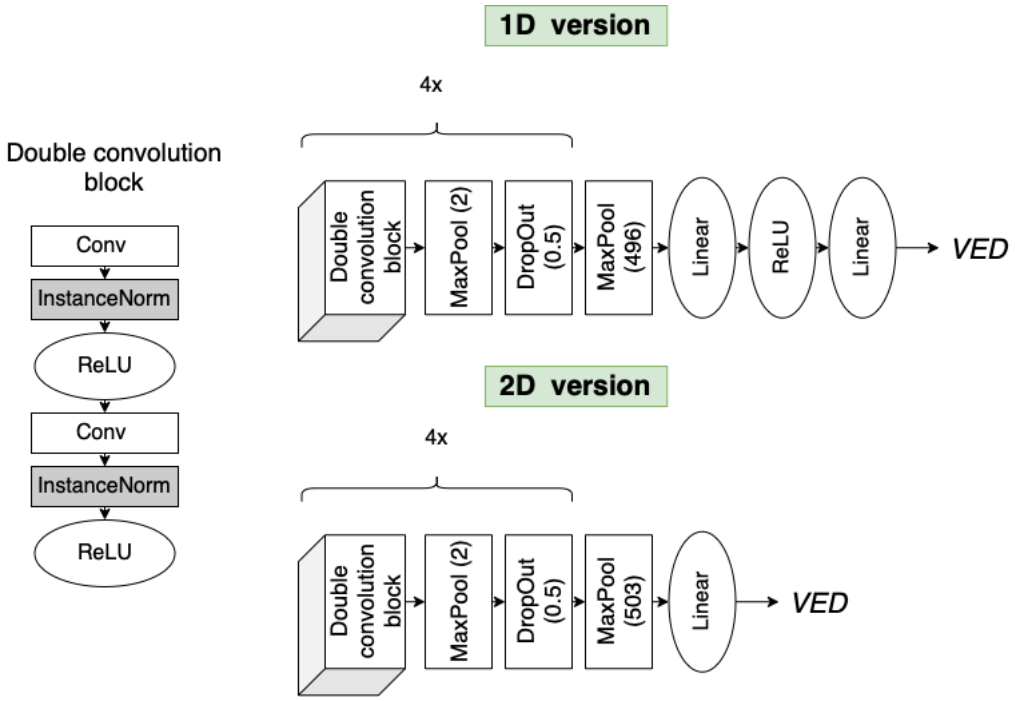


Fig. 10.2: 1D and 2D convolutional network architectures for assessment of Ventricular Electrical Dyssynchrony (VED) level.

Both models were trained using L1 loss and Adam optimization, with an initial learning rate of 0.001; a scheduler was also used to change the learning rate during training, with a reduction of 0.1 every 10th epoch. For both the 1D and 2D variants, early stopping was used during training, so if there was no improvement of the loss function on the validation dataset after 5 consecutive epochs, the training process was stopped.

## 10.3 Results

The performance of our models is measured based on the Mean Absolute Error between the actual and estimated VED values (MAE), along with the standard deviation (STD) and the Median Absolute Error (Median AE) on the test dataset. Results are reported separately for spontaneous ECG signals and for paced ones (Table 10.2) for 1D CNN and Table 10.3 for 2D CNN) and also for the negative and positive values of VED (Table 10.4) for 1D CNN and Table 10.5 for 2D CNN). To observe relationships between annotated and predicted VED we used scatter plots (Fig 10.3) and Spearman correlation coefficient (Table 10.6) since the data are not normally distributed according to the Shapiro Wilk test ($p<0.05$).

Tab. 10.2: Results for 1D CNN for VED assessment. MAE stands for mean absolute error STD for standard deviation and MEDIAN AE for median average error.

| | **MAE [ms]** | **STD [ms]** | **MEDIAN AE [ms]** |
|---|---|---|---|
| **Overall** | 12.61 | 18.95 | 8.25 |
| **Spontaneous** | 9.11 | 13.11 | 5.92 |
| **Paced** | 14.87 | 21.87 | 9.88 |

Tab. 10.3: Results for 2D CNN for VED assessment. MAE stands for mean absolute error STD for standard deviation and MEDIAN AE for median average error.

| | **MAE [ms]** | **STD [ms]** | **MEDIAN AE [ms]** |
|---|---|---|---|
| **Overall** | 12.27 | 17.73 | 8.58 |
| **Spontaneous** | 8.97 | 12.77 | 6.48 |
| **Paced** | 14.41 | 20.09 | 9.99 |

Tab. 10.4: Results for 1D CNN for positive and negative VED level.

| | **MAE [ms]** | **STD [ms]** | **MEDIAN AE [ms]** |
|---|---|---|---|
| **Positive VED** | 10.68 | 15.59 | 7.39 |
| **Negative VED** | 16.11 | 20.21 | 10.06 |

Tab. 10.5: Results for 2D CNN for positive and negative VED level.

| | **MAE [ms]** | **STD [ms]** | **MEDIAN AE [ms]** |
|---|---|---|---|
| **Positive VED** | 9.08 | 12.73 | 6.17 |
| **Negative VED** | 17.70 | 17.21 | 13.21 |

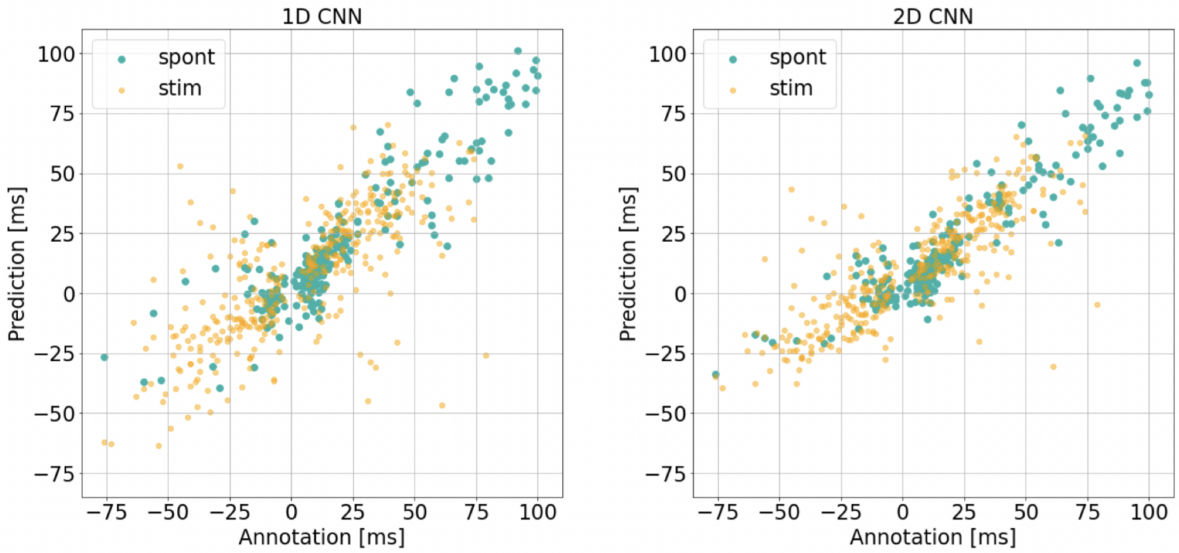


Fig. 10.3: Scatter plot of annotated vs estimated values of VED for 1D and 2D CNN for both spontaneous (spont green) and paced (stim yellow) UHF-ECG signals.

Tab. 10.6: Spearman correlation coefficients for scatter plots (Fig. 10.3) between annotated and estimated VED, reported for the whole test set and also separately for spontaneous and paced data. All correlation coefficients in the table have $p<0.0001$.

| **Pearson correlation coefficient** | | |
|---|---|---|
| | **1D CNN** | **2D CNN** |
| **Overall** | 0.83 | 0.85 |
| **Spontaneous** | 0.89 | 0.88 |
| **Paced** | 0.77 | 0.81 |

We also measured inference time for a single 8-second ECG block using the GPU (CUDA acceleration, GTX 1080 Ti). The average computing time (1000 trials) was 5.2 ±6.3 ms for both 1D and 2D CNN.

## 10.4 Discussion

Our results in terms of MAE (1D CNN - 12.61 ±18.95 ms, 2D CNN - 12.27 ±17.73 ms) and inference time (5.2 ±6.3 ms) suggest that the 1D and 2D CNN models provide very similar performance in the same amount of time. According to Mann Whitney test the null hypothesis cannot be rejected and the randomly selected value

of MAE in 1D CNN is assumed to be equal to the randomly selected value of MAE in 2D CNN ($p > 0.05$). Thus, our assumption that 2D convolution will yield improved results is not confirmed.

Both models achieve higher accuracy and hence smaller MAE on spontaneous data compared to the paced data (Tab. 10.2, 10.3. Also, the models perform better on positive VED values compared to negative ones (Tab. 10.4, 10.5), which corresponds to the percentage of negative values of VED in the training set (35%).

We also tried to evaluate the performance with signals that contained only major morphological group of QRS complexes (n = 402) in the 8s window, since our annotations for the VED value originate from the major morphological group. MAE is 11.85 ±18.39 ms and 11.42 ±16.49 ms for 1D and 2D CNN, respectively. Thus, there was only a marginal improvement of less than 1 ms.

If we look at the Spearman correlation coefficient and scatter plots between actual and estimated VED, a strong and significant positive correlation can be seen for both models and also for spontaneous and paced data. The 2D CNN model acquires a higher correlation (0.85 compared to 0.83 for 1D CNN) which can be observed particularly for paced data (0.81 for 2D CNN vs. 0.77 for 1D CNN).

However, comparison to other techniques to measure electrical dyssynchrony cannot be done since they do not exist. Still, we can point to advantages over a measure of interventricular mechanical delay, which is the closest possible option. The most commonly used technique for evaluating interventricular dyssynchrony is standard echocardiography which measures interventricular mechanical delay and delayed motion of the posterior wall. Study [47] shows that intra and inter observer reproducibility of this measure in 95% confidence interval is (-27,26 ms) and (-43,41 ms), respectively. If we look at the results of our models, which in this case predict a slightly different parameter, namely electrical ventricular dyssnyhcrony, the MAE of less than 13 ms indicates a smaller error than in the case of the measurement of mechanical dyssynchrony. And since our method is a model with fixed structure and properties, it is perfectly reproducible in comparison to a human expert.

Our results suggest that both models can estimate VED for spontaneous data, but performance for paced ECGs needs to be further improved. This could be achieved in the future either by augmenting this type of data during training, alternatively, suppression of the pacing stimuli will be necessary. The advantage over the current method [2] for VED estimation lies in the minimal signal pre-processing. Also, our method estimates the VED from an 8-second window, whereas the current solution in VDI Vision software estimates the VED from a 2-minute segment of the signal. VED estimation using deep learning is fast but requires refinement. Another advantage is that it works on 1 kHz sampled signals, so it can be used also on conventional ECG data, no UHF-ECG is required.

# Conclusion

The master thesis was aimed to research the issue of ventricular activation disorders (especially LBBB and RBBB) and the analysis of the UHF-ECG using methods of artificial intelligence, namely deep learning models. Generally speaking, the goal was to observe whether specific UHF-ECG analysis tasks can be solved via deep learning methods.

The first task was to design, implement and test a deep learning model suitable for the detection of QRS complexes in UHF-ECG and consider the possibility of simultaneous QRS complex width detection. We presented 2 real-time deep learning models, the first for QRS detection and the second for QRS detection focusing on its onset and offset and thus delivering QRS duration in one inference step. With minor changes in the architecture hyperparameters, and training (loss function, annotations) we were able to improve the performance of our QRS detection model. We received an overall F-score of 98.84 $\pm$0.51% for the QRS detection task. In terms of the QRS duration task, we received an overall Mean Absolute Error of 12.25 $\pm$2.16 ms.

An important benefit of the presented solution is a significantly increased F-score (98.84%) for the test dataset compared to the QRS detector (90.43%) embedded in the current version of the VDI Vision software suggesting that the average time for UHF- ECG analysis can be shortened. Thanks to minimal signal preprocessing and high detection performance, the presented model is likely to be implemented in the future generation of real-time VDI Vision software. The most beneficial effect for patients is shorter measurement time, which is essential during implant procedures. Another benefit is the simultaneous estimation of QRS duration, which is one of the parameters important for patient selection for CRT and rather raw measure of pacing effectivness.

Next, we developed a deep learning regression model (pix2pix network) to remove pacing stimuli from the UHF-ECG. We evaluated model performance based on the Spearman correlation of high-frequency amplitude envelopes in 15 frequency bands between the model output and the target. We found that on spontaneous data, the model provides higher correlation than on paced data and also that as the frequency band increases, there is a degradation in performance for both stimulated and spontaneous data. The advantage over the current method implemented in current version of VDI Vision is the stimuli removal in one inference step and no need of prior QRS detection. However, for the model to be implemented in VDI Vision, the performance of the model on paced data must reach at least the same performance as on spontaneous data.

The last task was the estimation of ventricular electrical dyssynchrony (VED),

for which we used 2 regression models: 1D CNN and 2D CNN. The MAE between our solution and ground truth is 12.61 $\pm$18.95 ms and 12.27 $\pm$17.73 ms for 1D and 2D CNN, respectively. MAE on spontaneous data is approximately 5 ms better than on paced data for both models, indicating the need to remove the pacing stimuli from the UHF-ECG. If we wanted to compare the estimation of VED with another parameter, the closest option would be standard echocardiography measuring interventricular mechanical delay. Our model of fixed structure and parameters has perfect reproducibility compared to a human observer measuring the mechanical dyssynchrony (intra observer reproducibility 95% CI is -27 - 26 ms) [47].

The advantage of all of these models lies in minimal signal preprocessing and delivering the desired output in one inference step. But while presented methods perform perfectly in case of QRS detection and segmentation, we also identified weak points in pacemaker stimuli removal and VED estimation methods. However, all these observations are essential for further development of UHF-ECG analysis, helping to state which specific methods could be changed to artificial intelligence approaches.

# Bibliography


[1] Cardiovascular Disease (CVDs). 2021. Available at URL: <https://www.who.int/news-room/fact-sheets/detail/cardiovascular-diseases-(cvds)>.

[2] Jurak P. et al. Ventricular dyssynchrony assessment using ultra-high frequency ECG technique. In *Journal of Interventional Cardiac Electrophysiology*, 2017, vol. 49, no. 3

[3] Plesinger F. et al. Ventricular Electrical Delay Measured From Body Surface ECGs Is Associated With Cardiac Resynchronization Therapy Response in Left Bundle Branch Block Patients From the MADIT-CRT Trial. In *Circulation: Arrhythmia and Electrophysiology*, 2018

[4] Plesinger F. et al. VDI Vision - Analysis of Ventricular Electrical Dyssynchrony in Real-Time. In *Computing in Cardiology (CinC)*, 2021

[5] Scientific Image and Illustration Software. BioRender. Available at URL: <https://www.biorender.com/>.

[6] Ward J.; Linden R. Physiology at a Glance. London: King's college, 2008. ISBN 978-1-4051-7723-8.

[7] Dubin D. Rapid Interpretation of EKG's. 2019. ISBN 0-912912-06-5.

[8] Oberman R.; Bhardway A. Physiology, Cardiac. In *StatPearls*, 2022

[9] Priest B. T.; McDermott J. S. Cardiac ion channels. In *Channels*, 2015, vol. 9, no. 6, pp. 352–9

[10] Grant A. O. Cardiac ion channels. In *Circ Arrhythm Electrophysiol*, 2009, vol. 2, no. 2, pp. 185–94

[11] Mornstein V. Lékařská fyzika a biofyzika. Brno: Masarykova univerzita, 2018. ISBN 978-80-210-8984-6.

[12] Halamek P.; Jurak P.; Jurco J.; Plesinger F. UHF Solver 1.3 - RIV - TA CR Starfos. 2017, Available at URL: <https://starfos.tacr.cz/cs>.

[13] O'Keefe J.H.; Hammill S.C.; Freed M. Complete Guide to ecgs. Bartlett Learning, 2021. ISBN 978-07-637-6405-0.

[14] Francia P.; Balla C.; Panei F.; Volpe P. Left Bundle-Branch Block—Pathophysiology, Prognosis, and Clinical Management. In *Clin. Cardiol*, 2007, vol. 30, no. 3, pp. 110–5

[15] Hampton J.R. ECG in practice (4th ed.). Churchill Livingstone, 2003. ISBN 978-80-247-1448-6.

[16] Auricchio A.; Lumens J.; Prinzen FW. Does cardiac resynchronization therapy benefit patients with right bundle branch block: cardiac resynchronization therapy has a role in patients with right bundle branch block. In *Circ Arrhythm Electrophysiol*, 2014, vol. 7, no. 3, pp. 532–4

[17] Henin M. et al. Indications of Cardiac Resynchronization in Non-Left Bundle Branch Block: Clinical Review of Available Evidence. In *Cardiol Res*, 2020, vol. 11, no. 1, pp. 1–8

[18] 2021 ESC Guidelines on Cardiac Pacing and Cardiac Resynchronization Therapy of the European Society of Cardiology. In *European Heart Journal*, 2021

[19] Andrla P.; Plesinger F.; Halamek J.; Leinveber P.; Viscor I.; Jurak P. A Method for Removing Pacing Artifacts from Ultra-high-frequency Electrocardiograms. In *Computing in Cardiology (CinC)*, 2018

[20] Plesinger F. et al. Robust multichannel QRS detection. In *Computing in Cardiology (CinC)*, 2014

[21] Plesinger F.; Jurco J.; Halamek J.; Leinveber P.; Reichlova T.; Jurak P. Mulltichannel QRS Morphology Clustering - Data Preprocessing for Ultra-High-Frequency ECG Analysis. In *CProceedings of the 3rd International Congress on Cardiovascular Technologies*, 2015, pp 11-8

[22] Curilla K. et al. Both selective and nonselective His bundle, but not myocardial, pacing preserve ventricular electrical synchrony assessed by ultra-high-frequency ECG. In *Hear. Rhythm*, 2020, vol. 17, no. 4, pp. 607–7

[23] Cholllet F. Deep Learning with Python. Manning Publications Co, 2018. ISBN 978-80-247-3100-1.

[24] LeCun Y. et al. Gradient-based learning applied to document recognition. In *Proceedings of the IEEE*, 1998, vol. 86, no. 11, pp 2278-2324

[25] Nejedly P.; Ivora A.; Smisek R.; Viscor I.; Koscova Z.; Jurak P.; Plesinger F. Classification of ECG using ensemble of residual CNNs with attention mechanism. In *Computing in Cardiology (CinC)*, 2021, vol. 48, pp 1-4

[26] Attia Z. I. et al An artificial intelligence-enabled ECG algorithm for the identification of patients with atrial fibrillation during sinus rhythm: a retrospective analysis of outcome prediction. In *Lancet*, 2019, vol. 394, pp 861-7

[27] Attia Z. I. et al. Screening for cardiac contractile dysfunction using an artificial intelligence–enabled electrocardiogram. In *Nat. Med.* , 2019, vol. 25, pp 70-4

[28] Koscova Z.; Ivora A.; Nejedly P.; Halamek J.; Jurak P.; Matejkova M.; Leinveber P.; Znojilova L.; Curila K.; Plesinger F. QRS Complex Detection in Paced and Spontaneous Ultra-High-Frequency ECG. In *Computing in Cardiology (CinC)*, 2021

[29] Plesinger F.; Jurco J.; Halamek J.; Jurak P. SignalPlant: an open signal processing software platform. In *Physiol. Meas.*, 2016, vol. 37, no. 7, pp. N38–N48

[30] Jan J. Číslicové zpracování a analýza signálu. Brno, 2010. ISBN 978-80-214-4018-0.

[31] Ronneberger O.; Fischer P.; Brox T. U-Net: Convolutional Networks for Biomedical Image Segmentation. In *International Conference on Medical image computing and computer-assisted intervention*, 2015, Springer, Cham, pp. pp. 234-7

[32] Moskalenko V.; Zolotykh N.; Osipov G. Deep Learning for ECG Segmentation," in Advances in Neural Computation. In *Advances in Neural Computation*, 2019, Machine Learning, and Cognitive Research III

[33] Kingma D. P.; Ba J. L. Adam: A Method For Stochastic Optimization. In: *ICLR*, 2015

[34] Zhilu Z.; Sabuncu Z.; Mert R. Generalized Cross Entropy Loss for Training Deep Neural Networks with Noisy Labels. In *arXiv*, 2018

[35] Welcome to Python.org. Available at URL: <`https://www.python.org/`>.

[36] Pytorch.org. Available at URL: <`https://www.python.org/`>.

[37] Pan J.; Tompkins W. J. A Real-Time QRS Detection Algorithm. In *IEEE Transactions of Biomedical Engineering*, 1985, vol. BME-32, no. 3

[38] Aro A.L. et al. Intraventricular Conduction Delay in a Standard 12-Lead Electrocardiogram as a Predictor of Mortality in the General Population. In *Circulation: Arrhythmia and Electrophysiology*, 2011, vol. 4, no. 5, pp. 704–710

[39] Koscova Z.; Smíšek R.; Nejedly P.; Halamek J.; Jurak P.; Leinveber P.; Curila K.; Plesinger F. Ultra-high Frequency ECG Deep-learning Beat Detector Delivering QRS Onsets and Offsets. In *Computing in Cardiology (CinC)*, 2022

[40] Goldberger A. et al. PhysioBank, PhysioToolkit, and PhysioNet: Components of a new research resource for complex physiologic signals. In *Circulation*, 2000, vol. 101, no. 23, pp. 215-220

[41] Kalyakulina A. et al. Lobachevsky University Electrocardiography Database. In *PhysioNet*, 2021, version 1.0.1

[42] Zusterzeel R. et al. FThe 43rd International Society for Computerized Electrocardiology ECG initiative for the automated detection of strict left bundle branch block. In *Journal of Electrocardiology*, 2018, vol. 51, no. 6, pp. 25-30

[43] Smisek R. et al. Fully automatic detection of strict left bundle branch block. In *Journal of Electrocardiology*, 2018, vol. 51, no. 6, pp. 31-34

[44] Zareba W. et al. Effectiveness of Cardiac Resynchronization Therapy by QRS Morphology in the Multicenter Automatic Defibrillator Implantation Trial-Cardiac Resynchronization Therapy (MADIT-CRT). In *Circulation*, 2011, vol. 123, no. 10, pp. 1061-1072

[45] Plesinger F. et al. The VED meter — a new tool to measure the ventricular conduction abnormalities in heart failure patients. In *CinC*, 2017, pp. 1-4, doi: 10.22489/CinC.2017.377-059

[46] Jurak P. et al. An additional marker of ventricular dyssynchrony. In *CinC*, 2015, pp. 77-80, doi: 10.1109/CIC.2015.7408590

[47] Burri H. et al. Poor agreement of echographic measures of ventricular dyssynchrony. In *European Journal of Echocardiography*, 2008, vol. 9, no. 2, pp. 235-240, doi: 10.1016/j.euje.2007.03.026

[48] Isola P. et al. Image-to-Image Translation with Conditional Adversarial Networks. In *CoRR*, 2016, doi.org/10.48550/arXiv.1611.07004

# Symbols and abbreviations

| | |
|---|---|
| **1D** | 1 Dimensional |
| **2D** | 2 Dimensional |
| **AI** | Artificial Intelligence |
| **AV** | Atrio Ventricular |
| **BBB** | Bundle Branch Block |
| **CHD** | Congenital Heart Disease |
| **CI** | Confidence Interval |
| **CNN** | Convolutional Neural Network |
| **CRT** | Cardiac Resynchronization Therapy |
| **CUDA** | Compute Unified Device Architecture |
| **DCM** | Dilated Cardiomyopathy |
| **DL** | Deep Learning |
| **ECG** | Electrocardiogram |
| **EF** | Ejection Fraction |
| **FNKV** | University Hospital Královské Vinohrady |
| **FNUSA** | St. Anne's University Hospital Brno |
| **GPU** | Graphical Processing Unit |
| **HF** | Heart Failure |
| **HFrEF** | Heart Failure with reduced Ejection Fraction |
| **IHD** | Ischemic Heart Disease |
| **LBB** | Left Bundle Branch |
| **LBBB** | Left Bundle Branch Block |
| **LVH** | Left Ventricular Hypertrophy |
| **MAE** | Mean Absolute Error |

| | |
|---|---|
| **MedAE** | Median Absolute Error |
| **MI** | Myocardial Infarction |
| **ML** | Machine Learning |
| **NYHA** | New York Heart Association |
| **PE** | Pulmonary Embolism |
| **PPV** | Positive Predctive Value |
| **QRSd** | QRS duration |
| **RBB** | Right Bundle Branch |
| **RBBB** | Right Bundle Branch Block |
| **RCS** | Randomized Clinical Studies |
| **ReLU** | Rectified Linear Unit |
| **SA** | Sinoatrial |
| **STD** | Standard Deviation |
| **VDI** | Ventricular Dyssynchrony Imaging |
| **VED** | Ventricular Electrical Dyssynchrony |
| **UHFDYS** | Ultra-high frequency Dyssynchrony |
| **UHF-ECG** | Ultra-high frequency ECG |
| **UHFQRS** | Ultra-high frequency QRS |